

RESEARCH ARTICLE

10.1002/2015JB012016

Key Points:

- Degree-2 positive geoid anomalies can be produced over chemically dense piles
- Chemically dense piles have a compensation effect on the surface geoid
- Thermochemical piles have a passive and secondary effect on large-scale convective structure

Correspondence to:

X. Liu,
xi.liu@colorado.edu

Citation:

Liu, X., and S. Zhong (2015), The long-wavelength geoid from three-dimensional spherical models of thermal and thermochemical mantle convection, *J. Geophys. Res. Solid Earth*, 120, doi:10.1002/2015JB012016.

Received 7 MAR 2015

Accepted 27 MAY 2015

Accepted article online 30 MAY 2015

The long-wavelength geoid from three-dimensional spherical models of thermal and thermochemical mantle convection

Xi Liu¹ and Shijie Zhong¹

¹Department of Physics, University of Colorado Boulder, Boulder, Colorado, USA

Abstract The Earth's long-wavelength geoid anomalies have long been used to constrain the dynamics and viscosity structure of the mantle in an isochemical, whole mantle convection model. However, there is strong evidence that the seismically observed large low shear velocity provinces (LLSVPs) in the lower mantle underneath the Pacific and Africa are chemically distinct and likely denser than the ambient mantle. In this study, we have formulated dynamically self-consistent 3-D spherical mantle convection models to investigate how chemically distinct and dense piles above the core-mantle boundary may influence the geoid. Our dynamic models with realistic mantle viscosity structure produce dominantly spherical harmonic degree-2 convection, similar to that of the present-day Earth. The models produce two broad geoid and topography highs over two major thermochemical piles in the lower mantle, consistent with the positive geoid anomalies over the Pacific and African LLSVPs. Our geoid analysis showed that the bottom layer with dense chemical piles contributes negatively to the total geoid, while the layer immediately above the chemical piles contributes positively to the geoid, canceling out the effect of the piles. Thus, the bottom part of the mantle, as a compensation layer, has zero net contribution to the total geoid, and the thickness of the compensation layer is ~1000 km or 2 to 3 times as thick as the chemical piles. Our results help constrain and interpret the large-scale thermochemical structure of the mantle using surface observations of the geoid and topography, as well as seismic models of the mantle.

1. Introduction

The Earth's nonhydrostatic geoid provides important constraints on the structure and dynamics of the mantle [e.g., Hager and Richards, 1989; Ricard et al., 1993]. The geoid is controlled by both the interior density variations and the dynamic topography of the surface and core-mantle boundary (CMB) [e.g., Pekeris, 1935; Hager and Richards, 1989]. The dynamic topography is caused by mantle flow and has a strong dependence on, thus can constrain, the mantle viscosity profile [e.g., Hager and Richards, 1989]. An important feature of the geoid is its dominantly degree-2 structure with two geoid highs above Africa and the central Pacific [e.g., Lerch et al., 1983] (Figure 1a).

Seismic tomographic studies also reveal two large low shear velocity provinces (LLSVPs) in the lower mantle below Africa and the Pacific Ocean surrounded by seismically fast, circum-Pacific anomalies [e.g., Dziewonski, 1984; Tanimoto, 1990; Masters et al., 1996; Ritsema et al., 1999] (Figures 1b and 1c), which correlate well with the long-wavelength geoid [e.g., Hager et al., 1985]. The seismic anomalies are often interpreted as purely due to the thermal effect in an isochemical, whole mantle convection framework, and the LLSVPs are thought as hot and buoyant roots of the "superplumes" that extend to the upper mantle, form the upwelling part of the global mantle convection, and cause the African and Pacific superswell topography [e.g., Marty and Cazenave, 1989; Davies and Pribac, 1993; Lithgow-Bertelloni and Silver, 1998; Romanowicz and Gung, 2002]. Representing the seismic structures as mantle density and buoyancy structure in the purely thermal, whole mantle convection model, geodynamic studies have not only reproduced the Earth's geoid but also provided constraints on the mantle viscosity structure [e.g., Hager and Richards, 1989].

In the past 20 years, however, various evidence suggest that the LLSVPs may be chemically distinct [e.g., Su and Dziewonski, 1997; Masters et al., 2000; Wen et al., 2001; Ni et al., 2002; He and Wen, 2009; Houser et al., 2008]. The anticorrelation between shear wave and bulk sound speeds in the LLSVPs suggests a thermochemical origin for the seismic heterogeneities in these regions [e.g., Masters et al., 2000]. The sharp seismic velocity contrasts at the edges of LLSVPs are better explained as features of chemically distinct

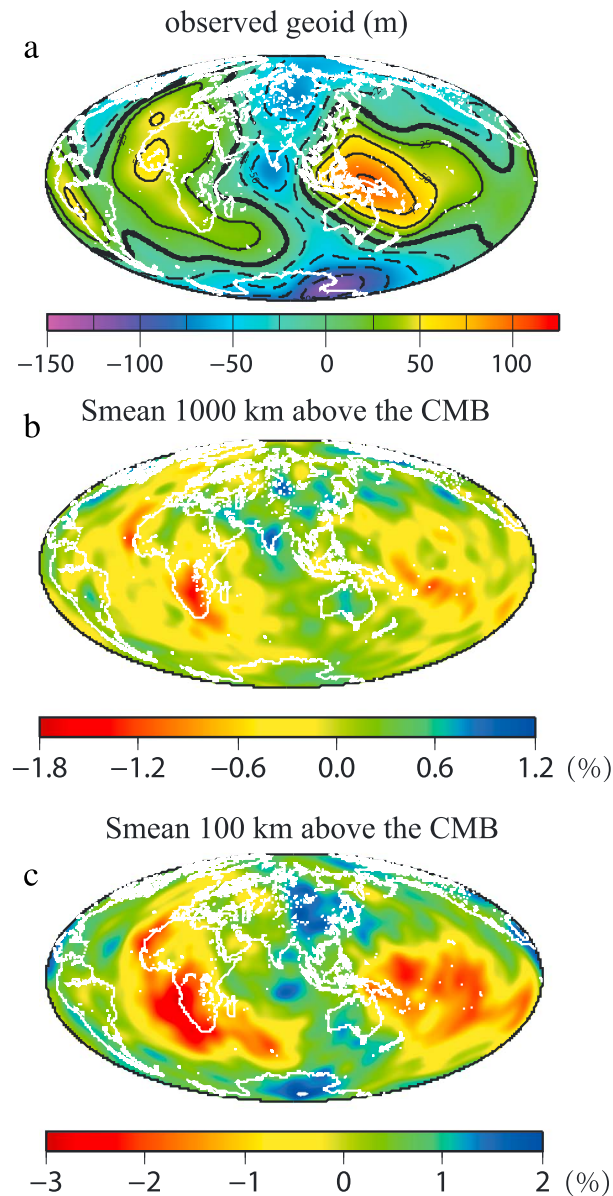


Figure 1. (a) The observed geoid up to degrees and orders 12 and seismic *S* wave anomalies at (b) 1000 km and (c) 100 km above the CMB from Smean model [Becker and Boschi, 2002], respectively.

the interface has opposite contribution to the geoid, compared to that below the interface. Through a joint inversion of the geoid and seismic data with a parameterization of possible compositional effect on the buoyancy, Forte and Mitrovica [2001] concluded that the LLSVPs are overall positively buoyant. Steinberger and Torsvik [2010] formulated thermochemical mantle flow models for the geoid and true polar wander, ignoring the buoyancy in the bottom 300 km thick layer of the mantle to account for possible compositional buoyancy effects.

However, these models have a number of drawbacks and assumptions that may limit their applications. Hager and Richards's [1989] model assumed that the chemically distinct layer is global and that the topography at the compositional interface is significantly smaller than the layer thickness. This assumption is inconsistent with seismic observations and thermochemical convection models showing that the LLSVPs or chemical piles only exist in isolated regions above the CMB with hundreds of kilometers topography [e.g., Wang and Wen, 2004; He and Wen, 2009; McNamara and Zhong, 2005a].

piles rather than purely thermal anomalies [Wen et al., 2001; Ni et al., 2002]. The thermochemical characteristics of the LLSVPs may also reconcile geochemical inferences of chemically distinct "reservoirs" that explain the difference between the oceanic island basalt and the mid-ocean ridge basalt [e.g., Hofmann, 1997; Kellogg et al., 1999; Kunz et al., 1998]. However, it should be pointed out that a number of recent studies have suggested that these seismic and geochemical observations could be explained as purely thermal and postperovskite phase change effects [Davies et al., 2012; Schuberth et al., 2009, 2012; Huang and Davies, 2007], thus questioning the necessity of interpreting the LLSVPs as chemical piles.

The large-scale chemically distinct piles, if they represent the LLSVPs as proposed [e.g., Garnero and McNamara, 2008], may have significant effects on the mantle dynamics. It has been suggested that thermochemical structures in the mantle affect the buoyancy force distribution, mantle flow configuration, and convective heat transfer [e.g., Tackley, 1998; Kellogg et al., 1999; Davaille, 1999; McNamara and Zhong, 2005a; Zhang et al., 2010]. However, the effects of thermochemical structures on the geoid are not well understood. Hager and Richards [1989] modeled a layered mantle convection with a compositional interface at a fixed radial location that represents the top surface of the chemically distinct *D* layer or the 670 km discontinuity. They showed that while density anomalies at the compositional interface do not produce any geoid anomalies (i.e., they are fully compensated), a density anomaly above

Buoyant LLSVPs or thermochemical piles suggested by *Forte and Mitrovica* [2001] may be inconsistent with the geochemical evidence for primitive chemical reservoirs or piles that would require the reservoirs to be negatively buoyant to avoid being mixed and recycled. However, this argument may depend on mantle mixing process [*Huang and Davies, 2007; van Keken et al., 2001*]. In *Steinberger and Torsvik's* [2010] model, the removal of mantle buoyancy from the bottom 300 km thick layer is rather ad hoc.

The goal of this study is to examine the effects of chemical piles (e.g., the LLSVPs) on the geoid as well as whether positive geoid anomalies in largely degree-2 convection as for the present-day Earth can be generated above primitive chemical piles above the CMB in dynamically self-consistent mantle convection models. A key in formulating dynamically self-consistent convection models to investigate the effects of thermochemical piles on the Earth's geoid is to generate long-wavelength convective structure with two major thermochemical piles above the CMB. This is accomplished here by modeling thermochemical convection [e.g., *McNamara and Zhong, 2004a*] with modestly strong lithosphere and a weak upper mantle [*Zhong et al., 2007*]. Our models represent the first mantle geoid models that include realistic mantle viscosity and dynamically generated degree-2 mantle structure, although semidynamic models with imposed surface plate motions could produce the degree-2 mantle structure [e.g., *McNamara and Zhong, 2005a*]. Our models indicate that positive geoid anomalies can be generated over two major thermochemical piles above the CMB in largely degree-2 mantle convection, similar to what is observed for the Earth. We also found that for the degree-2 geoid, the buoyancy from a large fraction of the bottom mantle (~1000 km in thickness) including the chemically dense piles has zero net contribution to the geoid, due to compensation effects. The paper is organized as follows. The next section describes the modeling methods for time-dependent convection models. Section 3 presents the modeling results, while discussions and conclusion are given in sections 4 and 5.

2. Model

2.1. Governing Equations, Initial, and Boundary Conditions

The time-dependent, dynamically self-consistent thermochemical convection models are formulated in a 3-D spherical shell geometry to study the effects of thermochemical structures on the geoid. The mantle is assumed to be an incompressible fluid, and under assumptions of the Boussinesq approximation and constant thermodynamic parameters except for the viscosity, the nondimensional governing equations for the conservation laws of the mass, momentum, energy, and composition are [*Tackley, 1998; McNamara and Zhong, 2004b; Zhong et al., 2008*]

$$\nabla \cdot \mathbf{u} = 0, \quad (1)$$

$$-\nabla p + \nabla \cdot [\eta(\nabla \mathbf{u} + \nabla^T \mathbf{u})] + Ra(T - BC)\mathbf{e}_r = 0, \quad (2)$$

$$\frac{\partial T}{\partial t} + (\mathbf{u} \cdot \nabla)T = \nabla^2 T + \gamma, \quad (3)$$

$$\frac{\partial C}{\partial t} + (\mathbf{u} \cdot \nabla)C = 0, \quad (4)$$

where \mathbf{u} is the velocity vector, p is the dynamic pressure, η is the viscosity, \mathbf{e}_r is the unit vector of the radial direction, Ra is the Rayleigh number, T is the temperature, B is the buoyancy number, C is the composition field, t is the time, and γ is the internal heat production rate. The detailed formulation and nondimensionalization of the equations can be found in *Zhong et al.* [2008].

The Rayleigh number Ra in equation (2) controls convective vigor and is defined as

$$Ra = \frac{\rho_0 g_0 \alpha_0 R^3 \Delta T}{\eta_0 \kappa_0} \quad (5)$$

where subscript 0 means reference values, ρ is the density, g is the gravitational acceleration, α is the thermal expansion coefficient, R is the radius of the Earth, ΔT is the temperature difference across the mantle, and κ is the thermal diffusion. Note that the Earth's radius, instead of mantle thickness, is used as the length scale to nondimensionalize the governing equations, and our Ra is ~10 times larger than defined by mantle thickness [e.g., *Zhong et al., 2000*].

Our thermochemical models only consider two compositions that differ in intrinsic density. C measures the mantle composition, with $C=0$ for the regular mantle and $C=1$ representing the denser component. The buoyancy number B measures the relative strength between the compositional and thermal buoyancy and is defined as

$$B = \frac{\Delta\rho_c}{\alpha_0\rho_0\Delta T} \quad (6)$$

where $\Delta\rho_c$ is the intrinsic density difference between the denser and regular mantle materials.

All models are in the 3-D spherical shell geometry. The top and bottom boundaries represent the surface and core-mantle boundary (CMB) and have dimensionless outer and inner radii $r=1$ and $r=0.55$, respectively. The models use free slip as well as isothermal boundary conditions at the top and bottom boundaries with fixed temperatures of 0 and 1, respectively. For the thermochemical convection, no composition flux is allowed to cross the top and bottom boundaries. The initial temperature field is a largely degree-3 structure. The initial condition for composition, which is only relevant for thermochemical models, is a denser layer with a uniform thickness of 400 km above the CMB. The volume of this dense layer is generally consistent with what is inferred for the LLSVPs [e.g., *Hernlund and Houser, 2008; Wang and Wen, 2004*]. As we are only interested in quasi steady state solutions, our results are insensitive to initial conditions.

We use a 3-D finite element convection package CitcomS to solve the governing equations for spherical shell mantle convection [*Zhong et al., 2000, 2008*]. The particle ratio method is employed in CitcomS to solve thermochemical convection problems [*McNamara and Zhong, 2004a; Tackley and King, 2003*]. Parallel computing techniques are implemented in CitcomS [*Zhong et al., 2000*]. The mantle is divided into 12 caps, and each cap is further divided to be run on multiple CPUs. Calculations presented in this study use 48, 96, or 192 CPUs. Models are typically computed for 20,000–50,000 time steps until heat flux reaches a quasi steady state with a relatively stable convective structure.

2.2. Viscosity Structure

The viscosity is both depth- and temperature-dependent, following a nondimensional rheological equation [*Zhong et al., 2007*]

$$\eta = \eta_0(z)\exp(E(T - T_0)) \quad (7)$$

where $\eta_0(z)$ is a depth-dependent prefactor, E is the activation energy, and $T_0=0.5$ is the reference temperature, which is approximately the mantle interior temperature in the models. E is set at 6.9078 that gives rise to 3 orders of magnitude in viscosity variations due to temperature changes from the surface to the CMB.

Since the Earth's geoid has a strong power at degree 2, our convection models are designed to produce long-wavelength, especially dominantly degree-2 convection. Generation of long-wavelength convective structure in dynamically self-consistent convection models has been an important topic in geodynamics. *Bunge et al.* [1996] reported that a viscosity increase of a factor of 30 from the upper to lower mantles as suggested from the geoid studies [e.g., *Hager and Richards, 1989*] increases convective wavelength but only up to a dominantly degree-6 structure. *McNamara and Zhong* [2005b] found that a moderately strong lithosphere leads to dominantly degree-1 convection (i.e., the longest possible wavelength in a spherical shell) for moderate Rayleigh numbers Ra . *Zhong et al.* [2007] further demonstrated that long-wavelength convection including that of degree 1 can be generated for Earth-like Rayleigh number by considering both moderately strong lithosphere and a viscosity increase at the 670 km depth. Some recent studies produced similar long-wavelength convection, also using modestly strong lithosphere [e.g., *Li et al., 2014a; Coltice et al., 2012*]. Following *Zhong et al.* [2007], we adjust the viscosity contrast between the lithosphere and the upper mantle to generate convection with different planforms, from dominantly degree-1, –2 to shorter wavelengths. Fixing $\eta_0(z)$ as 1 for the lower mantle and 1/30 for the upper mantle, but varying $\eta_0(z)$ in the lithosphere, denoted as $\eta_{litho}(z)$, we manage to build dominantly degree-2 convection models for both purely thermal and thermochemical convection. It should be noted that our temperature-dependent viscosity, while producing mobile lid convection, does not produce “plate-like” surface motions [e.g., *Ratcliff et al., 1997*]. Pseudo plastic rheology may lead to plate-like surface motions in mantle convection [e.g., *Moresi and Solomatov, 1998; Coltice et al., 2012*]. However, it remains a significant challenge

Table 1. The Thermodynamic Parameters

Parameters	Value
Earth's radius, R	6370 km
Mantle thickness, h	2870 km
Gravitational acceleration	9.8 m s^{-2}
Mantle density	3300 kg m^{-3}
Thermal diffusivity	$1 \times 10^{-6} \text{ m}^2 \text{ s}^{-1}$
Thermal expansion	$3 \times 10^{-5} \text{ K}^{-1}$
Temperature difference	2700 K
Specific heat	$10^3 \text{ m}^2 \text{ s}^{-2} \text{ K}^{-1}$

to reconcile observational, laboratory, and theoretical studies on rheological properties of lithosphere [e.g., *Zhong and Watts, 2013*].

2.3. Calculations of the Geoid and Dynamic Topographies

The geoid anomalies represent gravitational potential anomalies at the surface, φ , which can be obtained by solving the Poisson's equation

$$\nabla^2 \varphi = -4\pi G \delta \rho, \quad (8)$$

where G is the gravitational constant and $\delta \rho$ includes both density variations in the interior mantle and those associated with dynamic topographies at the surface and CMB. Here the interior density anomaly $\delta \rho$ is, in general, given by

$$\delta \rho = -\alpha \rho_0 \delta T + \Delta \rho_c C, \quad (9)$$

where δT is the temperature anomaly and C denotes the composition field.

The dynamic topographies at the surface and the CMB, denoted as s and b , respectively, can be related to the radial stresses at these boundaries as [*Zhong et al., 2008*]

$$s = -\frac{\sigma_{rr,t}}{\Delta \rho_t g}, \quad (10)$$

$$b = \frac{\sigma_{rr,b} + \rho_{\text{core}} \varphi_b}{\Delta \rho_b g}, \quad (11)$$

where $\sigma_{rr,t}$ and $\sigma_{rr,b}$ are the radial stresses at the surface and CMB, respectively, which can be calculated by solving the Stokes' flow equations (i.e., equations (1) and (2)); $\Delta \rho_t$ and $\Delta \rho_b$ are the density contrast across the surface and CMB, respectively; ρ_{core} is the density of the core; and φ_b is the gravitational potential perturbation at the CMB. The topography computed from equation (10) in our study includes contributions from the whole mantle and is different from the classic definition of dynamic topography that only includes contribution from the sublithospheric mantle [e.g., *Hager and Richards, 1989*].

The geoid calculations incorporate the self-gravitation effects, although the equations presented above did not include this effect for simplicity. With the self-gravitation effect, an additional term $-\rho \delta g \rightarrow \mathbf{e}_r$ should be added to the left side of equation (2), where $\delta g = -|\nabla \varphi|$ is the perturbation to the radial gravity [e.g., *Zhong et al., 2008*]. An efficient approach to solve the momentum equation, dynamic topographies, gravitational potential, and geoid with the self-gravitation is to introduce a reduced pressure term [e.g., *Zhong et al., 2008*].

3. Results

In this section, we will present the results of convective structure and geoid for the time-dependent and dynamically self-consistent mantle convection models. Numerical models for both purely thermal and thermochemical mantle convection are computed at two different Rayleigh numbers ($Ra = 5 \times 10^7$ and 1.5×10^8). Constant thermodynamic parameters, except the viscosity, are used for all models (Table 1). The viscosity is both depth- and temperature-dependent, and the viscosity prefactor in the lithosphere, $\eta_{\text{litho}}(z)$, is explored to achieve a predominantly long-wavelength convective structure (e.g., degree 2). Numerical grids of 12×65^3 are used for the cases with $Ra = 5 \times 10^7$, and grids of 12×97^3 are used for the higher Ra cases. The internal heating γ (equation (3)) is 50 and 70 for $Ra = 5 \times 10^7$ and 1.5×10^8 , respectively, leading to internal heating ratios of approximately 50% for these cases (i.e., the core and mantle each contributes half of the surface heat flux). For the thermochemical models, the buoyancy number B is varied to generate relatively stable chemical piles above the CMB. In general, a small buoyancy number leads to rapid overturn and destruction of a chemical layer, while a large buoyancy number results in a stable chemical layer with a flat surface but no chemical piles [e.g., *McNamara and Zhong, 2004b; Oldham and*

Table 2. Time-Dependent, Self-Consistent Numerical Models^a

Case	Ra	B	η_{litho}	Steps	Grid	γ	Nu	Vt
Case 1	5×10^7	0	0.27	30,000	12×65^3	50	42	6470
Case 2	5×10^7	0.8	0.27	40,000	12×65^3	50	26	2580
Case 3	1.5×10^8	0	0.3	60,000	12×97^3	70	54	7060
Case 4	1.5×10^8	0.5	0.3	40,000	12×97^3	70	45	5150

^a Ra , B , η_{litho} , and γ stand for Rayleigh number, buoyancy number, viscosity prefactor in the lithosphere, and internal heating, respectively. Column steps show the maximum time steps for the case. The numbers 12 in column grid means 12 caps divided for the spherical shell and 65 and 97 mean the resolution for the longitude, latitude, and the radial directions, respectively. Nu and Vt are the nondimensional surface heat flux and surface RMS velocity after the model reaches quasi steady states.

Davies, 2004]. Our model calculations show that dominantly degree-2 structure can be generated for thermochemical models with $B=0.8$ and 0.5 for $Ra=5 \times 10^7$ and 1.5×10^8 , respectively. Because the primary interest of this study is on the geoid, we only present four cases that display dominantly degree-2 mantle structures, at two different Ra , each with thermal and thermochemical convection models.

3.1. A Purely Thermal Convection Model at $Ra = 5 \times 10^7$

In Case 1, the viscosity prefactors, $\eta_0(z)$, are 1, 1/30, and 0.27 for the lower mantle, upper mantle, and lithosphere, respectively (Table 2). Starting from a 3-D temperature with a dominantly degree-3 structure, the model quickly reaches a statistically steady state with dimensionless surface heat flux of ~ 42 (Figure 2a). The internal heating ratio is 44%. The power spectra of the temperature structure within the top thermal boundary layer (i.e., at a depth of 100 km) is used to characterize convective structure. For each spherical harmonic degree l , the power spectrum of a function f is

$$F_l = \sum_{m=0}^l \left[\left(f_{\text{cos}}^{lm} \right)^2 + \left(f_{\text{sin}}^{lm} \right)^2 \right], \quad (12)$$

where f_{cos}^{lm} and f_{sin}^{lm} are the cosine and sine coefficients of spherical expansion of the function f at degree l and order m , respectively. The power spectra as a function of time for degrees 1 to 4 for Case 1 are presented in

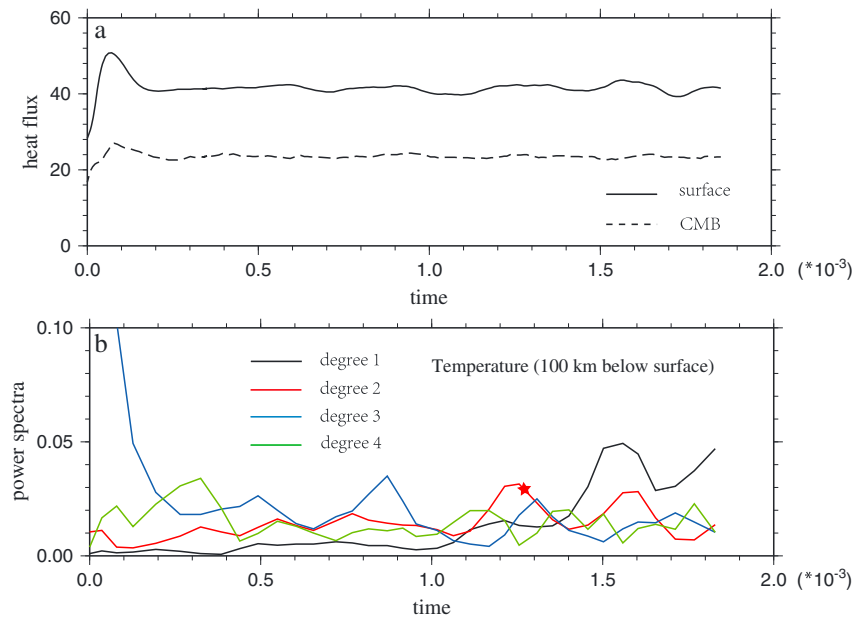


Figure 2. Time dependence of (a) the nondimensional surface (solid line) and CMB (dashed line) heat flux and of (b) the power spectra for temperature structure at 100 km depth for degrees 1 to 4, denoted by black, red, blue, and green lines, respectively, for Case 1. The red star in Figure 2b marks the time with a dominantly degree-2 convective structure that is used for the structure and geoid analyses. In Figure 2a, the CMB heat flux is plotted after taking into account of the surface area effect.

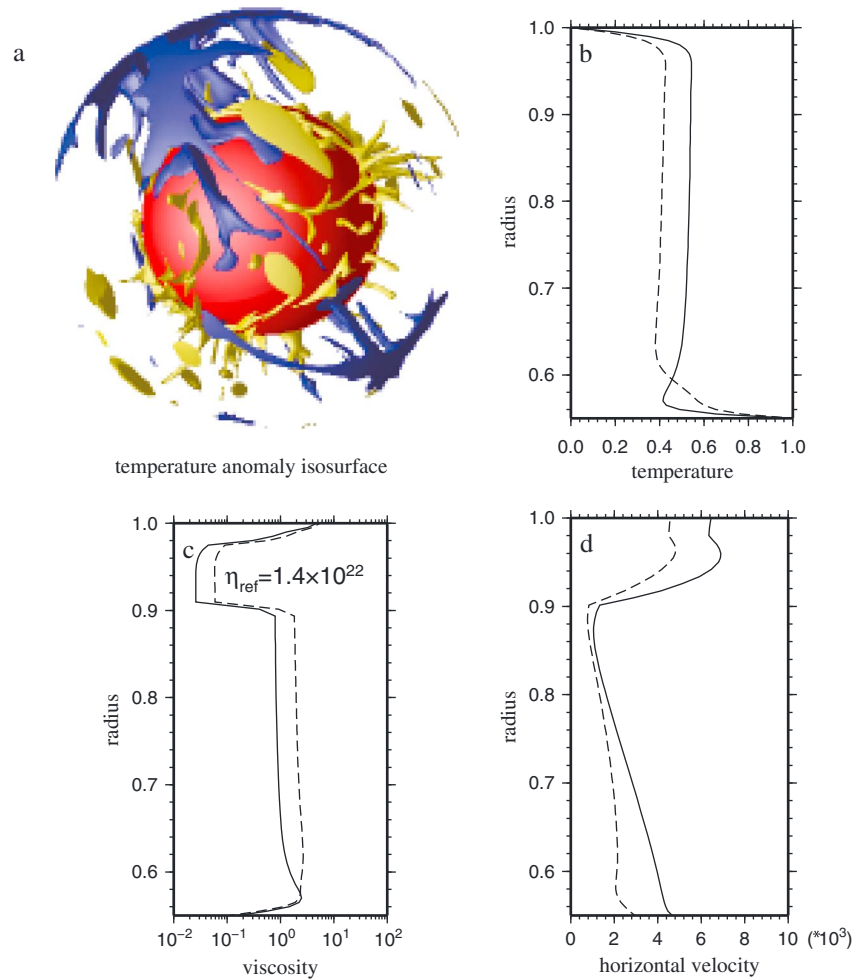


Figure 3. (a) The isosurface of temperature anomalies $\delta T = -0.2$ and $\delta T = 0.2$ in blue and yellow, respectively, for a representative snapshot of Case 1, horizontally averaged (b) temperature, (c) viscosity, and (d) horizontal velocity, for representative snapshots of both Case 1 (solid line) and Case 2 (dashed line). The reference viscosity is determined to be 1.4×10^{22} Pa s, using $Ra = 5 \times 10^7$ for Cases 1 and 2 and parameters in Table 1.

Figure 2b. Although the degree-1 convective structure becomes the strongest at the end, there is a significant time period during which degree-2 structure is significant.

A snapshot of a dominantly degree-2 convective structure (time marked in Figure 2b) is used for the geoid analysis. A 3-D isosurface plot for the temperature anomalies at this time step (Figure 3a) shows two clusters of downwellings and upwellings, which are indicative of a dominantly degree-2 structure, as also displayed in 2-D plots of temperature structure at a depth of 100 km (Figure 4a) and 100 km above the CMB (Figure 4b). Figure 3b shows the horizontally averaged temperature, indicating two well-developed thermal boundary layers (TBLs) at the surface and bottom. The horizontally averaged viscosity shows that the average lithospheric viscosity is ~ 60 times of the upper mantle viscosity, while the lower mantle viscosity is ~ 30 times larger than the upper mantle (Figure 3c). Scaled by parameters in Table 1, $Ra = 5 \times 10^7$ indicates a reference viscosity of $\sim 1.4 \times 10^{22}$ Pa s, and the lower mantle viscosity of $\sim 3 \times 10^{22}$ Pa s, which is comparable to that inferred from postglacial rebound study [Simons and Hager, 1997; Mitrović and Forte, 2004]. The root-mean-square (RMS) of the horizontal velocity indicates a mobile lid convection with surface velocity that is comparable to that in the upper mantle (Figure 3d).

Surface and CMB topographies as well as the surface geoid at the corresponding time are computed and scaled to dimensional values using physical parameters in Table 1 (Figures 4c–4e). Notice that the surface topographies presented in this study include contributions from both the top thermal boundary layer and

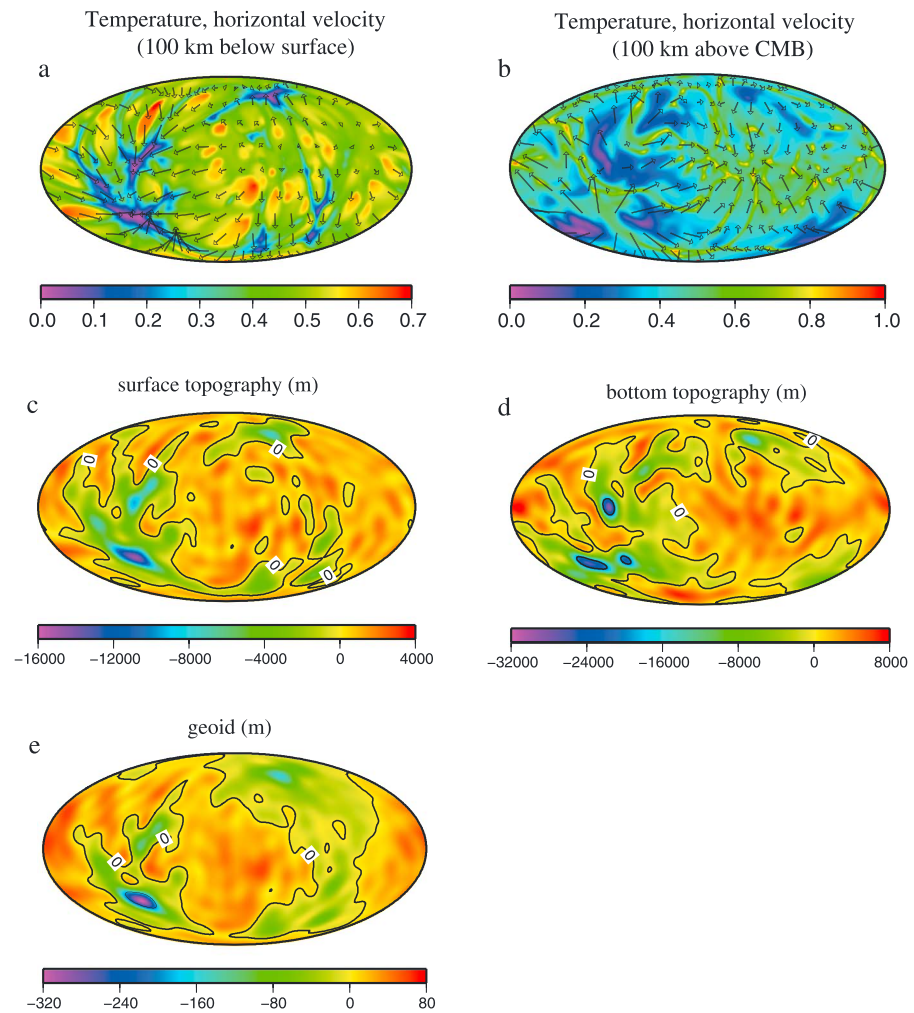


Figure 4. Temperature structures at (a) 100 km depth and (b) 100 km above the CMB, (c) the surface and (d) the bottom topographies, and (e) the surface geoid, all for Case 1. The arrows in both Figures 4a and 4b denote the horizontal velocities at corresponding depths. Contour lines of 0 m are plotted in Figures 4c–4e.

the underlying mantle, while dynamic topography typically excludes the contribution from the lithosphere (i.e., the top thermal boundary layer) [e.g., Hager and Richards, 1989], and the difference is presented in the discussion section. The topographies are well correlated with the convective structure and are negative in the cold downwelling regions and positive in hot upwelling regions. The negative topographies in downwelling regions have much larger magnitudes than the positive topographies over upwellings, due partly to the high viscosity associated with cold downwellings that tends to increase the coupling of downwellings to the top and bottom boundaries. The geoid is prevalently at long wavelengths with a dominantly degree-2 structure (Figures 4e and 5a). The long-wavelength geoid is positive over the two major upwelling regions and is negative elsewhere (e.g., major downwelling regions). The largest negative geoid of -320 m is above the center of one major downwelling, and its magnitude is 3 times larger than that of the maximum positive geoid of ~ 80 m. The general pattern of the positive geoid over two major upwelling systems from the model is consistent with the observed for the present-day Earth (Figure 1).

We now analyze the contribution of buoyancy at different depths to the surface geoid. Our mantle convection model employs 64 unevenly distributed elements in the radial direction. The geoid contributed from buoyancy at each of these 64 layers can be computed by solving the Stokes' flow equations for the topographies and then the Poisson's equation (equation (8)), using the buoyancy from that layer but the same 3-D mantle viscosity as in the global calculations. Using the same 3-D viscosity to compute the geoid (and topographies) from each element layer of buoyancy guarantees that the summation of the geoid

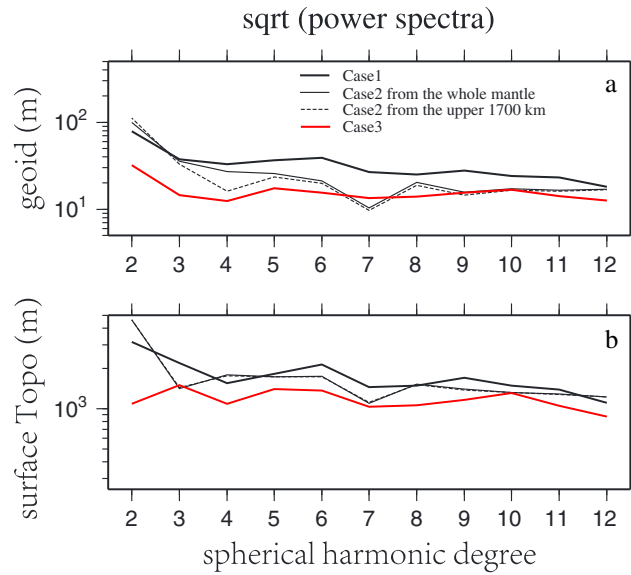


Figure 5. Square root of power spectra of (a) geoid and (b) surface topography at degrees 2–12 for Case 1 (solid black), Case 2 from the buoyancy of the whole mantle (thin black) and of the upper 1700 km of the mantle (thin dashed black), and Case 3 (red).

buoyancy at the middle mantle has significant short-wavelength structure (Figures 6d, 7d, and 7e), its geoid is still dominated by long wavelengths (Figures 6c and 7a), again due to attenuation effects that reduce short-wavelength structures. The normalized power spectra of the geoid from each depth (Figure 7a) show that degree-2 component is the strongest at nearly all depths except for the midmantle where degrees 3 and 4 are the strongest. Figure 7b shows the maximum geoid power among all the degrees at different depth that is used to normalize the power spectra as shown in Figure 7a. Figure 7b indicates that the top 300 km and the bottom 1000 km of the mantle contribute the most to the surface geoid, while the midmantle’s contribution is small.

The degree correlation C_l between the geoid from a unit thickness layer at each depth, h , and the total geoid H is computed for degrees 2–10 (Figure 7c) following

$$C_l = \frac{\sum_{m=0}^l (H_{\sin}^m h_{\sin}^m + H_{\cos}^m h_{\cos}^m)}{\sqrt{H_l h_l}}, \quad (13)$$

where h_l and H_l represent the power of h and H at degree l , respectively, which are computed by equation (12). The degree-2 correlation is mostly positive except at depth of ~600 km for all the degrees (Figure 7c), suggesting that the buoyancy at different depths mostly contributes positively to the surface geoid. Also note that the geoid power at ~600 km depth is small (Figure 7b).

3.2. A Thermochemical Convection Model With $Ra = 5 \times 10^7$

Case 2 is identical to Case 1 except for including a compositionally distinct material above the CMB with buoyancy number $B=0.8$ (Table 1), which corresponds to an intrinsic density difference of 210 kg/m³ relative to the normal mantle, using parameters in Table 1. The same initial temperature field as in Case 1 is used for Case 2, and initially the compositionally distinct material is uniformly distributed in a 400 km thick layer above the CMB. The model is computed for about 40,000 time steps and reaches a quasi steady state. The convective structure is dominated by long-wavelengths, similar to Case 1, suggesting that the chemically distinct material plays a relatively minor and passive role in forming convective structure in Case 2.

In Case 2, convective structure with dominantly degree-2 component persists for a long time (>2 Ga), and we choose a time step with a well-developed degree-2 structure for geoid analysis (Figure 8). Temperatures are high within and above two chemical piles, indicating that two major upwellings are formed above the piles (Figure 8a). The two chemical piles extend to ~400 km above the CMB, but their areal extent shrinks with

(and topographies) from all the layers is equal to the total geoid in Figure 4e, as the Stokes’ flow equations with a fixed 3-D viscosity are linear. The geoid from each element layer is further divided by the layer thickness to represent the geoid contributed from the layer per unit thickness (i.e., per kilometer). Figures 6a, 6c, and 6e show the geoid from three layers at depths of 200 km, 1400 km, and 200 km above the CMB. The corresponding buoyancy structures for the three layers are given in Figures 6b, 6d, and 6f, where the buoyancy is defined as $-\delta\rho = \alpha\rho_0\delta T - \Delta\rho_c C$, with a unit of kg/m³. While the buoyancy is comparable in both wavelengths and magnitude at the top and the bottom TBLs (Figures 6b, 6f, 7d, and 7e), the geoid from the top TBL is significantly larger than that from the bottom TBL (Figures 6a, 6e, and 7b) due to attenuation effects. Although the

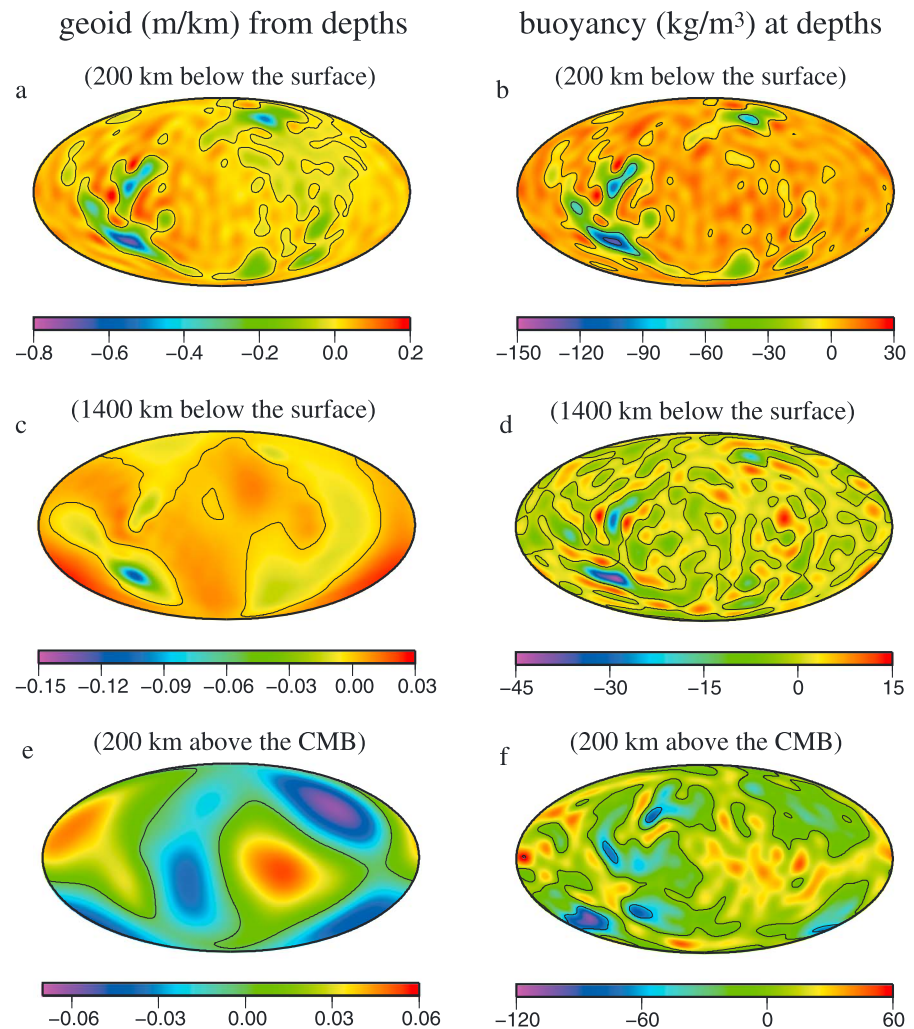


Figure 6. (a and b) The geoid produced by mantle buoyancy at 200 km depth, for those from (c and d) 1400 km depth, and for those at (e and f) 200 km above the CMB, all for Case 1. The buoyancy and the geoid are all given as per unit thickness (i.e., per kilometer). The contour lines of 0 are plotted in Figures 6a–6f.

distance from the CMB (Figures 8b and 8c). Considering that the chemical layer initially has a uniform thickness of 400 km, the configuration of the chemical piles (Figures 8b and 8c) suggests that their volume has been reduced significantly due to entrainment after long time integration. The entrained materials are dispersed throughout the mantle but do not seem to form any coherent structure to affect the large-scale mantle dynamics. The horizontally averaged temperature and horizontal velocity, as well as the viscosity contrast between the lithosphere and the upper mantle are smaller than those for the purely thermal model (Figures 3b–3d). Figures 9a and 9b show the temperature and horizontal velocity at a depth of 100 km and 100 km above the CMB. Two broad warm regions in the upper mantle occur above the two chemical piles, and the chemical piles above the CMB are separated by cold downwellings (Figures 9a and 9b). Horizontal velocities above the CMB indicate that there are two separated convective systems inside and outside the chemical piles (Figure 9b). Outside of chemical piles, the horizontal flow from downwellings reaches the piles' edge and continues along the upper boundary of the piles, introducing counter flow inside of the chemical piles due to shear coupling.

The surface topography is positive in two broad regions of upwellings over the chemical piles and is negative in downwelling regions (Figure 9c). The magnitude of the negative topography is up to 3 times that of the positive topography. The range of surface topography of Case 2 is reduced by ~40% compared with that of Case 1. However, the degree-2 topography is stronger in Case 2 than that in Case 1 (Figure 5b), due to a

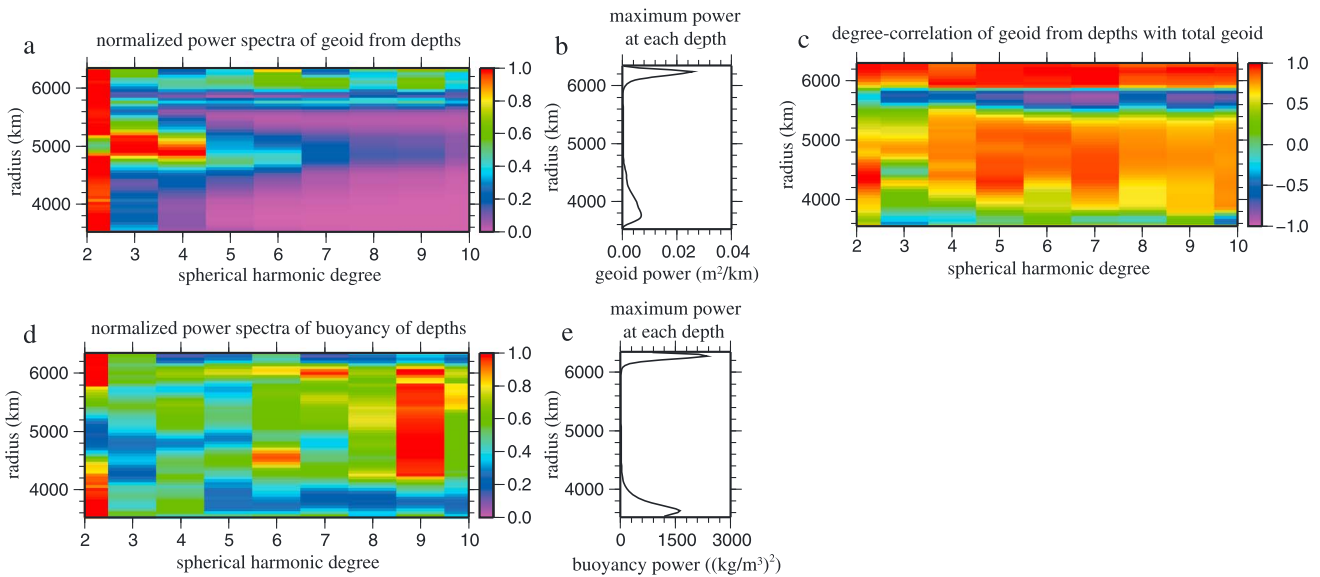


Figure 7. (a) The normalized power spectra of the geoid and (b) the maximum geoid power per unit thickness for degrees 2–10 produced from buoyancy at different depths, (c) the degree correlation for degrees 2–10 between the total geoid and the geoid contributed from each layer, and (d) normalized buoyancy spectra and maximum power (Figure 7c) at different depths, all for Case 1. Note that the maximum power at different depths in Figures 7b and 7e are used to normalize the power spectra shown in Figures 7a and 7d, respectively.

stronger degree-2 structure in Case 2. At the large scale (i.e., degrees 2 and 3), the surface topography is in the range of ± 3 km. The CMB topography under the chemical piles ranges from zero to slightly negative and is extremely smooth (Figure 9d). However, the most negative CMB topography occurs in the central regions of downwellings outside the piles, while the positive CMB topography is also outside the chemical piles (Figure 9d). Compared with Case 1, the amplitude of the negative CMB topography in Case 2 is also reduced significantly, as a result of compensation associated with the deformation of the chemical piles.

Two major positive geoid anomalies occur in the regions with positive surface topography above the chemical piles, while the long-wavelength negative geoid is in downwelling regions (Figure 9e). The geoid has the strongest power at degree 2 (Figure 5a). It is interesting to note that Case 2 resembles the present-day Earth’s scenario, in which the long-wavelength geoid and topography highs occur above the African and Pacific LLSVPs (or thermochemical piles) that are separated by circum-Pacific subducted slabs. Moreover, the large-scale geoid (degrees 2 and 3) of $\sim \pm 80$ m in Case 2 is close to that observed on the Earth. This suggests that the positive long-wavelength geoid anomalies in the Pacific and Africa are consistent with the interpretation of the two LLSVPs as chemically denser, possibly primitive thermochemical piles.

We repeat the geoid analysis for contribution from different depths as done for Case 1. The normalized power spectra of the geoid versus depth reveal that degree 2 is the strongest for almost all depths except at ~ 400 km above the CMB where degree 3 is the strongest (Figure 10a). Notice that at ~ 400 km above the CMB, the chemical piles largely disappear. The maximum power of the geoid is high in the lower mantle and is the largest at ~ 300 km above the CMB, within the radial extent of the chemical piles (Figure 10b), which is different from that in Case 1 of purely thermal convection (Figure 7b). This suggests that the chemical piles have an important effect on the geoid.

The degree correlation of the geoid from each depth with the total geoid shows high correlation in the upper mantle for all the degrees (Figure 10c), similar to Case 1 (Figure 7c). At degree 2, while the correlation is high and positive for the top ~ 2300 km of the mantle, the correlation is high but negative for the bottom ~ 400 km of the mantle (Figure 10c), which is different from that for Case 1. The negative correlations also exist for degrees 3 for the bottom 200 km of the mantle.

The negative correlation at degrees 2 and 3 between the geoid from buoyancy immediately above the CMB and the total surface geoid occurs where the chemical piles are, suggesting that the chemical piles may

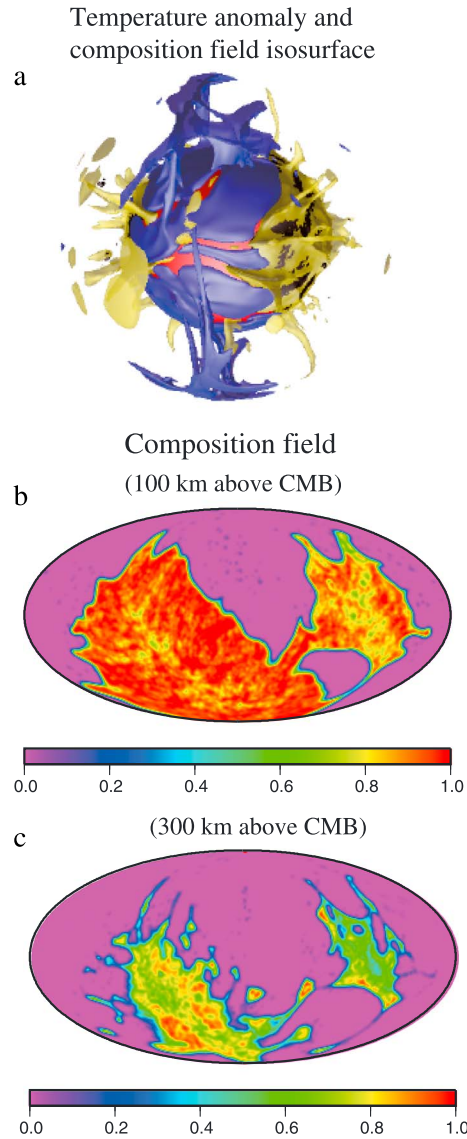


Figure 8. (a) The isosurface of temperature anomalies $\delta T = -0.2$ and $\delta T = 0.2$ in blue and yellow, respectively, for a representative snapshot of Case 2, and composition field at (b) 100 km and (c) 300 km above the CMB, respectively. In Figure 8a, the black isosurface below the upwelling plumes (i.e., yellow isosurfaces) represents chemical piles.

Therefore, the compensation effect is unique to thermochemical convection where the gravity anomalies from negatively buoyant chemical piles are offset and canceled by those from hot, buoyant normal mantle above the piles.

To further illustrate the compensation effect, we compute the geoid resulting from the buoyancy of the top ~ 1700 km of the mantle (i.e., ignoring the bottom 1200 km of the mantle), and the resulting geoid (Figure 12b) is quite similar to the geoid from using the whole mantle buoyancy (Figures 9e and 5a). At degree 2, the geoid from the top 1700 km of the mantle buoyancy correlates at $\sim 90\%$ but has $\sim 12\%$ larger amplitude than the original degree-2 geoid (Figure 5a). The amplitude difference results from both imperfect correlations at degree 2, which implies difference in degree-2 geoid patterns and finite radial numerical resolution. Although the compensation thickness of 1200 km is determined by considering the degree-2 geoid only (Figure 12a), the overall similarity between the geoid with and without the bottom

contribute negatively to the surface geoid. This is supported by analysis of the geoid from the buoyancy at 300 km (i.e., within the chemical piles) and 600 km (above the piles) above the CMB. At 300 km above the CMB, the buoyancy is negative within the piles and is dominantly degree 2 (Figures 11b and 10d). The resulting geoid is strongly degree 2 with two negative geoid anomalies over the piles (Figure 11a) and is negatively correlated with the total surface geoid at long wavelengths (Figures 9e and 10c). At 600 km above the CMB, while the buoyancy has significantly shorter wavelengths (Figure 10d), it is generally positive above the chemical piles (Figure 11d). The resulting geoid is positive over two broad regions approximately above the chemical piles (Figure 11c) and is positively correlated with the total surface geoid (Figures 9e and 10c).

The highly negatively correlated geoid from the layers within the chemical piles suggests that the geoid from these regions of the lower mantle may be canceled or compensated by the geoid from the mantle above the piles. We define the geoid contribution of the buoyancy from a unit thickness layer at a depth, denoted as h , to the total geoid H at degree l , R_l , as

$$R_l = \frac{\sum_{m=0}^l (H_{\sin}^{lm} h_{\sin}^{lm} + H_{\cos}^{lm} h_{\cos}^{lm})}{\sqrt{H_l H_l}}, \quad (14)$$

where all the variables are defined following equations (12) and (13). Equation (14) is valid when the magnitude of degree correlation between h and H at degree l is high, such as degree 2 (Figure 10b) in Case 2. The degree contribution R_2 (i.e., for degree 2) is plotted in Figure 12a. By integrating R_2 over radius from CMB upward, it is found that the bottom 400 km of the mantle with the chemical piles contributes $\sim -60\%$ to the total geoid at degree 2, and the negative contribution is cancelled by the geoid from an ~ 800 km thick layer right above the chemical piles. As a result, the bottom ~ 1200 km is fully compensated with no net contribution to the surface geoid at degree 2. The depth contribution to the total geoid for Case 1 is also plotted for comparison (Figure 12a), and no similar compensation effect exists for Case 1.

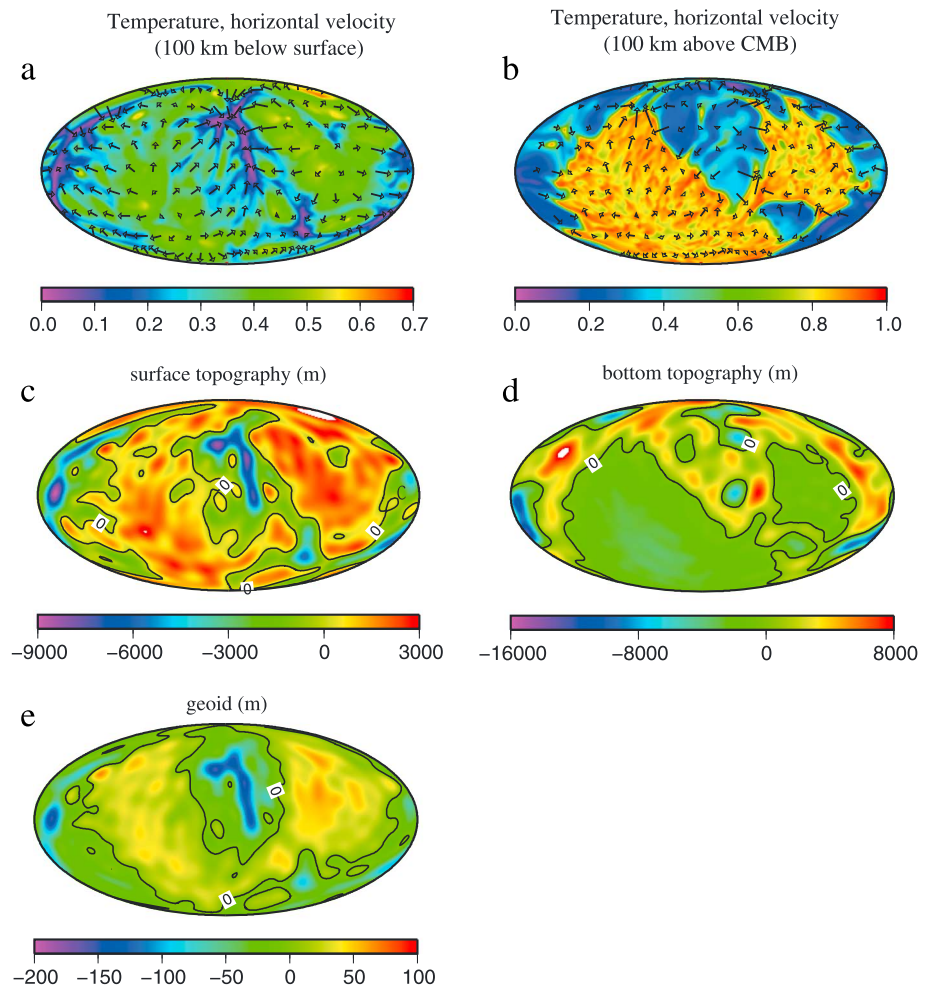


Figure 9. Temperature structures at (a) 100 km depth and (b) 100 km above the CMB, (c) the surface and (d) the bottom topographies, and (e) the surface geoid, all for Case 2. The arrows in both Figures 9a and 9b denote the horizontal velocities at corresponding depths. Contour lines of 0 m are plotted in Figures 9c–9e.

1200 km of the mantle structure arises because the geoid has the strongest power at degree 2 and also because the deep mantle tends to have small effects on the geoid at relatively short wavelengths (Figure 5a). Surface topography produced by the upper 1700 km of the mantle for Case 2 is nearly identical to that by the entire mantle (Figures 9c, 12c, and 5b), and the former has a total degree correlation of 99.9% with and a contribution of 99.7% to the later for degrees 1–12. Similar layer analysis for the surface topography to that for the geoid shows that the surface topography contributed from the upper part of the mantle has much stronger power than that from the bottom part of the mantle, and thus is insensitive to the lower mantle buoyancy structure.

Finally, it should be pointed out that numerical entrainment is inevitable in thermochemical convection calculations [e.g., *van Keken et al.*, 1997], and it often requires special attention such as high resolution using adaptive mesh refinement [e.g., *Leng and Zhong*, 2011; *Davies et al.*, 2007]. Compositionally dense material is constantly entrained and mixed with the normal fluid in thermochemical convection. This entrainment would eventually destroy the chemical heterogeneities and homogenizes the fluids [e.g., *Jellinek and Manga*, 2002; *Davaille*, 1999; *McNamara and Zhong*, 2004a]. However, numerical models tend to significantly overestimate the entrainment rates. The large numerical entrainment rate may reduce the size of chemical piles significantly faster than it should. To reduce the impact of numerical entrainment on the dynamics and the geoid analysis, we implement a scheme to redefine compositional field C to maintain the original compositional difference in our modeling. After we identify a certain time window in

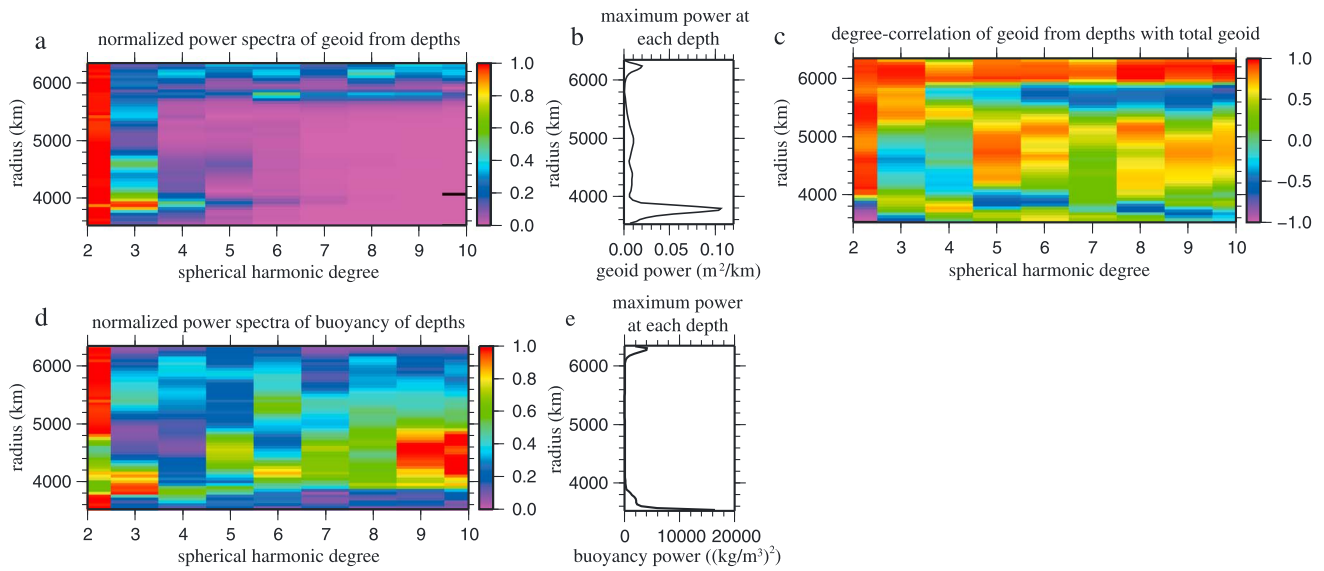


Figure 10. (a) The normalized power spectra of the geoid and (b) the maximum geoid power per unit thickness for degrees 2–10 produced from buoyancy at different depths, (c) the degree correlation for degrees 2–10 between the total geoid and the geoid contributed from each layer, and (d) normalized buoyancy spectra and maximum power (Figure 10c) at different depths, all for Case 2. Note that the maximum power at different depths in Figures 10b and 10e are used to normalize the power spectra shown in Figures 10a and 10d, respectively.

which the geoid analysis is to be performed, we redefine the compositional field C by assigning C to be either 1 or 0, depending whether or not the original C is larger than a threshold value (e.g., 0.5). Using the newly defined C , we recompute the models for ~ 5000 time steps over the time window of interest, and the geoid analysis is then performed for the time frames with the redefined compositional field. We found that the geoid results as presented above are insensitive to time steps.

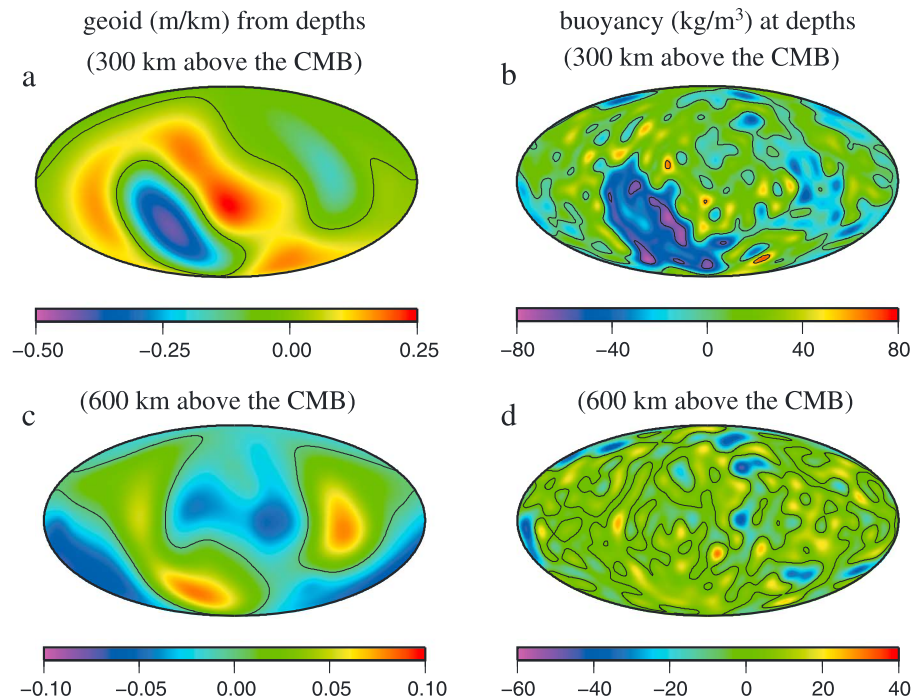


Figure 11. (a) The geoid produced by (b) mantle buoyancy at 300 km above the CMB (within the chemical piles), and for (c and d) the corresponding geoid and buoyancy from the layer at 600 km above the CMB (above the chemical piles), all for Case 2. The geoid in Figures 11a and 11c are given as per unit thickness (i.e., per kilometer).

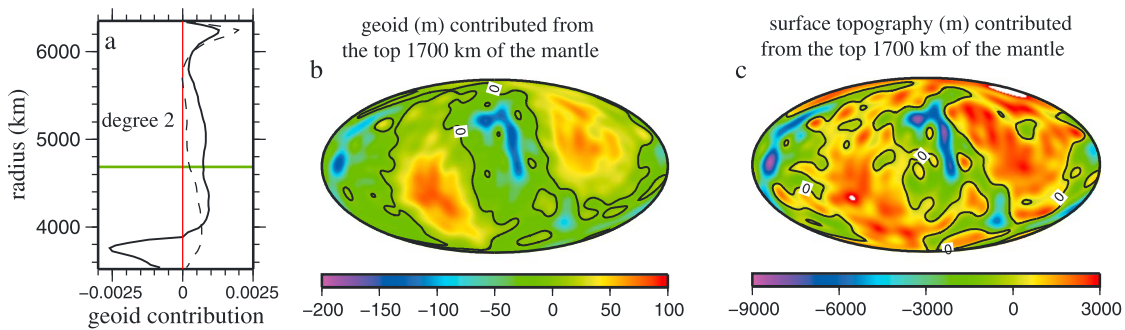


Figure 12. (a) The degree-2 contribution to the total geoid from the layer with unit thickness at different depths for both Case 2 (solid black line) and Case 1 (dashed black line), (b) the geoid, and (c) the surface topography contributed from the top 1700 km of the mantle of Case 2. In Figure 12a, the red line represents the reference value of 0 and the green line denotes the compensation region for Case 2, below which the net contribution to the total geoid is 0. The contour lines of 0 m are plotted in Figures 12b and 12c.

3.3. Models With $Ra = 1.5 \times 10^8$

Rayleigh number (Ra) controls the convection vigor and heat flux as well as surface convective velocity increase with Ra . The dimensionless quasi steady state averaged surface heat flux of Cases 1 and 2 are ~ 42 and ~ 26 , respectively, corresponding to a total surface heat flux of 30 TW and 18 TW, based on the parameters in Table 1. They both are significantly lower than the Earth's mantle convective heat flux of ~ 36 TW [e.g., Davies, 1999]. The surface RMS velocities for Cases 1 and 2, averaged for the degree-2 dominant quasi steady state, are 3.2 cm/yr and 1.3 cm/yr, respectively, and are smaller than the averaged present-day plate speed of ~ 4 cm/yr [Gordon and Jurdy, 1986]. The lower mantle viscosities for Cases 1 and 2 are about 10^{22} Pa s and $\sim 3 \times 10^{22}$ Pa s, respectively (Figure 3c), which are comparable with but still larger than that estimated from postglacial rebound [e.g., Simons and Hager, 1997]. Therefore, it is important to examine the possible effects of larger Ra on compensation effects seen in the thermochemical convection model of Case 2. To test such effects, we formulate both purely thermal and thermochemical convection models with $Ra = 1.5 \times 10^8$. It is found that the main results for models with intermediate Ra , as presented in sections 3.1 and 3.2, also hold for models with $Ra = 1.5 \times 10^8$. Cases with a higher Ra , however, seem to systematically reduce the dynamic topography and geoid, as presented below.

The initial temperature condition for the purely thermal convection model with $Ra = 1.5 \times 10^8$ (Case 3) is the same as in Case 1. Case 3 has viscosity prefactors of 0.3, 1/30, and 1 in the lithosphere, the upper mantle, and the lower mantle, respectively, which are also similar to those in Case 1 (Table 2). Measured by the temperature in the bottom TBL (e.g., 100 km above the CMB), a dominantly degree-2 convective structure is reached with two main downwelling systems (Figure 13a). However, unlike in Case 1 where the power spectra of the temperature within the top and bottom TBLs are similar, in Case 3, the temperature in the top TBL has stronger short-wavelength structures than that in the bottom TBL. Notice that with $\eta_{\text{litho}} \geq 0.4$, the models would reach a stable, dominantly degree-1 structure, measured from both the top and the bottom temperature fields [e.g., Zhong et al., 2007]. With the increased Ra , Case 3 has an averaged surface heat flux of ~ 54 (or 39 TW) and a surface RMS velocity of 7060 (or 3.5 cm/yr). The averaged lower mantle viscosity is 5×10^{21} Pa s.

Similar to Case 1, the CMB topography is dominantly degree 2 and is negative/positive below the downwelling/upwelling regions (Figure 13c). The surface topography shows strong short-wavelength components and is dominantly degree 3 (Figures 13b and 5b), following the pattern of the shallow depth temperature structure. The magnitude of the surface and CMB topographies is smaller than that of Case 1 due to a smaller mantle viscosity with the higher Ra for Case 3 (Figure 5b). The dominantly degree-2 geoid, dictated by the lower mantle structure, is positive in two broad regions approximately above the upwellings and is negative above the two main downwellings revealed in the bottom TBL temperature (Figures 13d and 5a). The buoyancy at different depths mostly contributes positively to the surface geoid across the mantle (Figure 14e). These results are similar to that for Case 1.

The thermochemical model, Case 4, has the same initial temperature and composition conditions as in Case 2 but uses $Ra = 1.5 \times 10^8$ and buoyancy number $B = 0.5$. Using the same viscosity prefactors as Case 3, Case 4

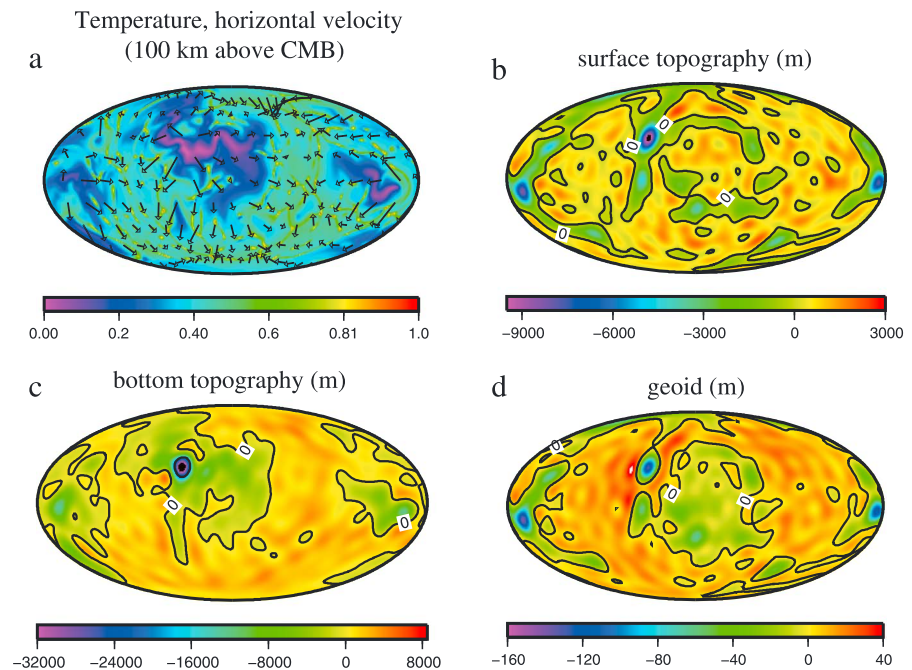


Figure 13. (a) The temperature structure at 100 km above the CMB, (b) the surface and (c) the bottom topographies, and (d) the geoid for Case 3. The arrows in Figure 13a denote the horizontal velocities at the corresponding depth. The contour lines of 0 m are plotted in Figures 13b–13d.

achieves a dominantly degree-2 convective structure. Similar to Case 2, two stable, hot thermochemical piles separated by two cold downwellings are formed (Figure 14a), and the piles extend to the height of ~ 600 km above the CMB. This again suggests that thermochemical piles do not have a significant effect on the dominant convective wavelength that is mainly controlled by viscosity structure. The surface heat flux and RMS velocity of Case 4 are ~ 32 TW and 2.6 cm/yr, respectively. The lower mantle viscosity is 5×10^{21} Pa s, which is similar with that of Case 3.

The CMB topography for Case 4 (Figure 14c) is relatively smooth in the pile regions, with one pile region slightly uplifted and the other one slightly depressed. Similar to Case 2, the lowest CMB topography occurs outside the piles at the center of one downwelling, and the highest topography is also outside the pile regions but near the piles. While the topographies are strongly influenced by the degree-2 convective structure, there are also significant short-wavelength components (Figures 14b and 14c). The topographies for Case 4 are smaller than those for Case 3 due to the compensation (or buffering) effect by the chemical piles and are also reduced from Case 2 due to a higher Ra .

The geoid for Case 4 is dominantly degree 2 and is positive in two broad regions approximately over the two chemical piles (Figure 14d). The geoid contributed from buoyancy with a unit thickness at different depths, the depth-dependent geoid power spectra, and degree correlations with the total surface geoid are computed, following the same procedures as for Cases 1 and 2. Both the power spectra and degree correlations are similar to those for Case 2. The layer contribution to the geoid at degree 2 indicates that the bottom ~ 600 km of the mantle, which is the vertical extent of the chemical piles, contributes negatively to the total geoid and that the negative contribution is compensated by the positive contribution from the mantle right above the piles (Figure 14e). The thickness of the compensation region is ~ 1100 km at degree 2, similar to that in Case 2. The geoid produced by the top ~ 1800 km of the mantle resembles the total geoid (Figures 14f and 14d), and it correlates at 94% and accounts for 114% of the total geoid, summed from degrees 2 to 12. Similar with Case 2, the surface topographies produced before and after removing the bottom part of the mantle are nearly identical (the correlation and contribution for degrees 1–12 are 99.9% and 101.4%, respectively). Based on Cases 2 and 4, we conclude that for thermochemical convection with heavy thermochemical piles, the bottom layer of the mantle does not

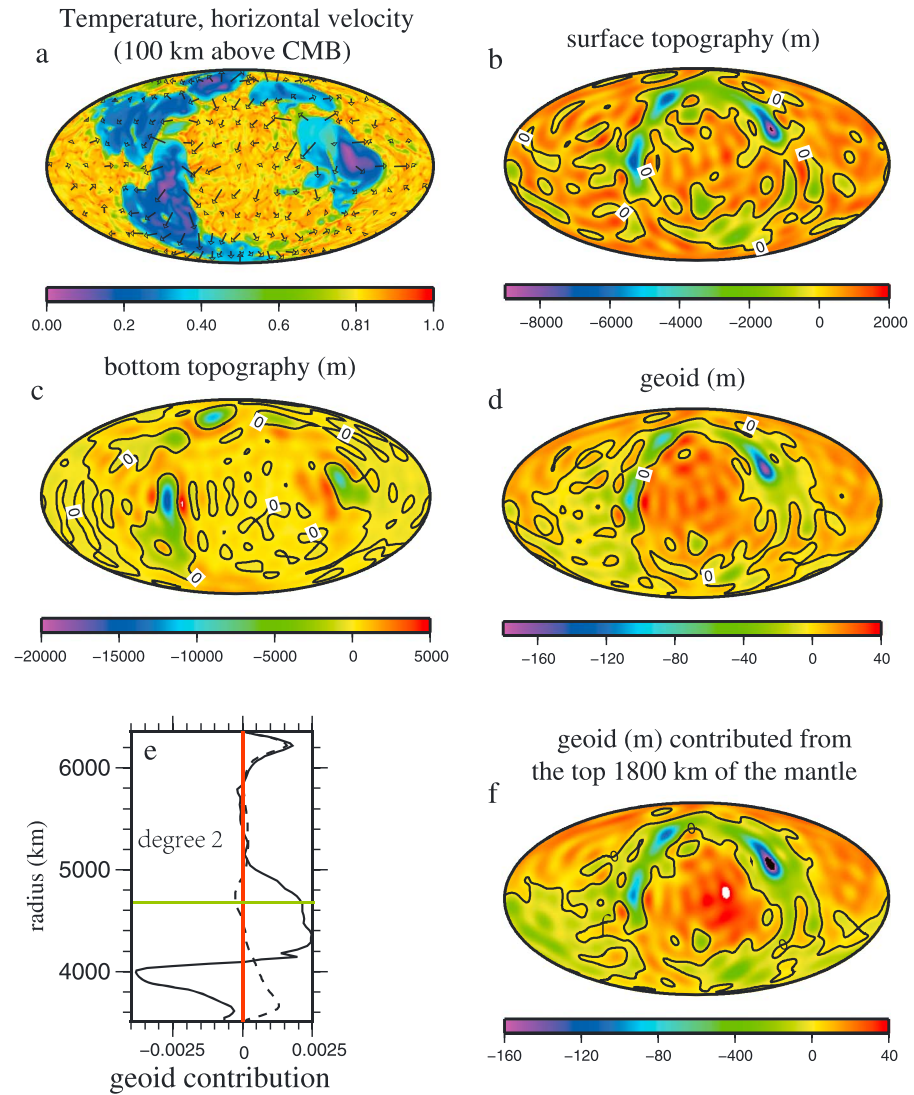


Figure 14. (a) The temperature structure at 100 km above the CMB, (b) the surface and (c) the bottom topographies, (d) the geoid, (e) the degree 2 contribution to the total geoid from the layer with unit thickness at different depths, and (f) the geoid from the top 1800 km of the mantle for Case 4. The arrows in Figure 14a represent the horizontal velocities at the corresponding depth. The black contours in Figures 14b, 14c, 14d, and 14f are for 0 m contours. In Figure 14e, the black dashed line is for degree-2 contribution for Case 3, the red line represents the reference value of 0, and the green line denotes the compensation region for Case 4, below which the net contribution to the total geoid is 0.

have net contribution to the geoid, as well as the surface dynamics topography, and this compensation layer thickness is ~1000 km for the chemical piles extending to ~500 km above the CMB.

4. Discussion

4.1. The Geoid, Thermochemical LLSVP, and Compensation Layer

In this study, we present dynamically self-consistent thermal and thermochemical convection models that generate dominantly degree-2 convective structure at Earth's mantle like Rayleigh number. The degree-2 convective structure from our dynamic models resembles the seismically observed mantle structure and is generated with a depth- and temperature-dependent mantle viscosity structure (e.g., a modestly strong lithosphere) that is consistent with that inferred from postglacial rebound and geoid studies. These dynamic models allow us to investigate the dynamic effects of thermochemical mantle structure on the long-wavelength geoid and topography anomalies. Our dynamically self-consistent thermochemical

convection models show that long-wavelength geoid and topography highs are produced above two chemically distinct and dense piles (Figures 9c and 9e). This may reconcile the observations of long-wavelength positive geoid and topography anomalies in the Pacific and Africa with the interpretation that the Pacific and Africa LLSVPs are chemically distinct and dense piles [e.g., *McNamara and Zhong, 2005b*]. This also supports the notion that the chemical piles as suggested seismically in the LLSVPs [*Masters et al., 2000; Wen et al., 2001; Ni et al., 2002*] may represent reservoirs for primitive mantle materials and also as the source materials for oceanic island basalts [*Hofmann, 1997; Boyet and Carlson, 2005*].

Our dynamically self-consistent models also show that the thermochemical piles have a compensation effect on the long-wavelength geoid and that the bottom ~ 1000 km of the mantle (i.e., a compensation layer) has nearly zero net contribution to the total geoid. The relatively thick compensation layer arises because the dense, negatively buoyant chemical piles above the CMB produce negative surface geoid, while the hot, buoyant mantle above the piles generates positive geoid, canceling the negative geoid from the chemical piles. In our models, the chemical piles reach to 400–500 km height above the CMB, and the thickness of the compensation layer is about 1000–1200 km or 2–3 times of the pile thickness. The compensation thicknesses in our study are determined based on the degree-2 geoid. While degree-2 geoid accounts for $>50\%$ of the geoid in both the observation and our models, the degree-3 geoid is also significant. Our dynamic models indicate that similar compensation effect also exists at degree 3 (Figure 10c), but the effect is not as evident and robust as that for the degree 2. For example, for Case 2 with $Ra = 5 \times 10^7$, the degree-3 compensation thickness ranges between 250 km and 500 km at different time steps.

It has been a challenge to construct mantle buoyancy structure from the seismic tomographic models for a chemical heterogeneous mantle because of the uncertainties in mantle seismic, composition, and mineral physics models. For example, *Forte and Mitrovica [2001]* suggested a limited role of composition in affecting seismic and density anomalies of the LLSVPs and concluded that the LLSVPs needed to be overall buoyant to fit the geoid. However, buoyant LLSVPs would not be in dynamic equilibrium with the ambient mantle to stay in the deep mantle as chemically distinct, possibly primitive mantle reservoirs. In their studies on the geoid and true polar wander, to consider possible chemical effects of the LLSVPs, *Steinberger and Torsvik [2010]* simply removed the bottom 300 km of the mantle where the LLSVPs are. Clearly the results on the geoid and compensation thickness from our time-dependent dynamic models differ significantly from these two studies based on instantaneous mantle flow. The compensation effect revealed from our dynamic models may offer an approach to construct mantle buoyancy structure from seismic models for calculating the geoid. That is, we may ignore mantle buoyancy in the compensation layer and only consider the upper part of the mantle (e.g., the top 1800 km). This approach avoids determining the conversion from seismic anomalies to buoyancy structure in the LLSVPs where seismic anomalies have both thermal and chemical origins. It should be pointed out that although reaching to >600 km heights above the CMB, the LLSVPs have the largest seismic anomalies ($>5\%$) only in the bottom ~ 300 km with a nonuniform structure [e.g., *Wang and Wen, 2004; He and Wen, 2012*]. This suggests that although our dynamic models suggest a reasonable estimate of the compensation thickness of ~ 1000 km, its exact thickness for the Earth's mantle is still somewhat uncertain, possibly ranging from 600 km to 1200 km.

4.2. Surface Topography, Dynamic Topography, and the Geoid

It is important to point out that surface topography presented in this study (e.g., Figure 4c) differs from the classic definition of dynamic topography. Dynamic topography is often defined as the topography caused by the mantle buoyancy excluding that from shallow depths (i.e., the lithosphere), revealing the dynamics of the mantle interiors [e.g., *Hager and Richards, 1989*]. With the classic definition, the subsidence caused by the plate cooling is not considered as dynamic topography. The surface topography in this study, on the contrary, is computed from the buoyancy structure of the whole mantle including the top thermal boundary layer (i.e., TBL or the lithosphere). Therefore, although the positive surface topography in our models is 3–4 km (e.g., Figures 4c and 9c), it should not be interpreted as a 3–4 km dynamic topography.

It is of interest to explore the surface dynamic topography of convective models using the classic definition. We will use Case 2 as an example. The top TBL of Case 2, determined from the horizontally averaged temperature (Figure 3a), is ~ 170 km thick. Figures 15a and 15b present the large-scale (i.e., the degrees 2 and 3) surface topography with and without the contribution from the top TBL, respectively. Note that the

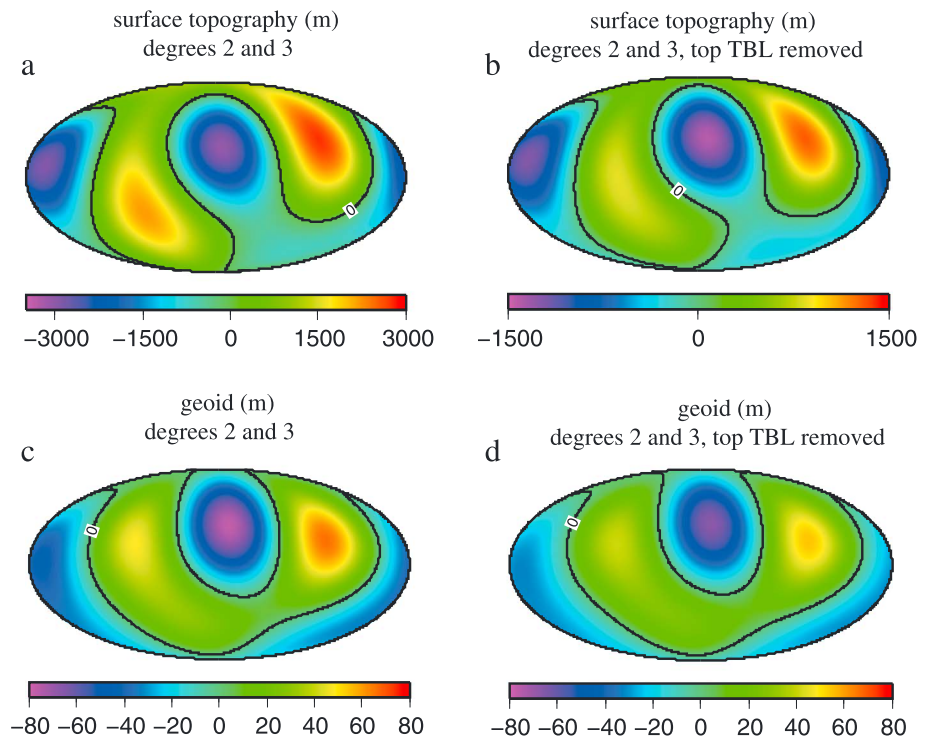


Figure 15. The degrees 2 and 3 surface topography for Case 2 (a) with and (b) without the contribution from the top 170 km thick thermal boundary layer, and the geoid (c) with and (d) without the contribution from the top thermal boundary layer. Surface topography in Figure 15b is the dynamic topography in its classic definition. Contour lines of 0 are plotted in Figures 15a–15d.

surface topography in Figure 15a is essentially the long-wavelength components of that in Figure 9c, while Figure 15b shows the dynamic topography in its classic definition. The dynamic topography is in a range of ± 1.5 km and is only half of the surface topography. That is, the top TBL contributes $\sim 50\%$ of the surface topography. However, the top TBL does not significantly influence the geoid (Figures 15c and 15d), contributing $\sim 15\%$ of the total geoid at degrees 2 and 3. This reflects the fact that the buoyancy at shallow depths is largely compensated with little effect on the geoid [e.g., Hager and Richards, 1989].

A similar analysis is done for other cases. For example, for Case 1, the long-wavelength dynamic topography (i.e., degrees 2 and 3) ranges from -1.5 km to 1 km, and the top 160 km TBL contributes $\sim 60\%$ to the surface topography. The dynamic topography for Case 4 is $\sim \pm 700$ m, and its 150 km thick top TBL contributes $\sim 40\%$ at degrees 2 and 3 to the total surface topography. The results further show that the surface topography and the dynamic topography are smaller for models with a larger Ra (i.e., smaller viscosity). It should be pointed out that in its classic definition, the dynamic topography of both purely thermal and thermochemical cases in our study is in a range of ± 1 km, which is comparable to that inferred from seismic models [e.g., Hager and Richards, 1989; Lithgow-Bertelloni and Silver, 1998], suggesting that our models use reasonable model parameters.

4.3. CMB Topography

Our dynamic models show that the CMB topography is distinctly different between purely thermal and thermochemical convection models. In purely thermal convection, the CMB topography shows variations at all different scales that correspond directly to mantle convective structure (e.g., Figures 4d and 13c). For example, in the upwelling regions, short-wavelength positive CMB topography with large amplitude below localized mantle plumes superposes on long-wavelength positive topography. However, for thermochemical convection, CMB topography in the chemical pile (i.e., upwelling) regions is extremely smooth and is nearly zero or slightly depressed/uplifted (Figures 9d and 14c), although the piles are chemically dense with net negative buoyancy (Figure 11b). However, the CMB topography varies

significantly and rapidly outside the pile regions where both the largest uplift and the largest depression occur. While the largest uplift occurs at the vicinity of the chemical piles, the largest depression is underneath the coldest downwellings. This is generally consistent with previous modeling studies using a similar mantle viscosity structure but imposed plate motions [Lassak *et al.*, 2010]. For Case 4 with Earth-like convective vigor, the largest positive and negative CMB topography are about 4 km and -10 km, respectively, and they exist over relatively small length scales (hundreds of kilometers) (Figure 14c). Recent analyses of short-period *PcP* seismic waves suggest up to 6 km depression of the CMB beneath Kenai Peninsula over several hundred kilometer length scales [Wu *et al.*, 2014]. Similar future seismic studies on the short-wavelength CMB topography may provide constraints on mantle dynamic models.

4.4. The Effects of 3-D Viscosity on the Geoid

Geoid modeling studies often assume a 1-D viscosity structure [e.g., Hager and Richards, 1989], because the simplified viscosity allows the use of the propagator matrix method to compute the geoid, making it possible for efficiently sampling model parameter space and inversion [e.g., King and Masters, 1992]. However, there has been a concern on how the simplified 1-D viscosity structure may introduce errors in the geoid for the mantle with 3-D viscosity [e.g., Richards and Hager, 1989]. For 3-D viscosity inferred from seismic tomography models, it seems that the effects from 3-D viscosity or lateral variations in viscosity (i.e., LVV) are only important at wavelengths smaller than those corresponding to spherical harmonic degree 4 [Zhang and Christensen, 1993]. This is generally consistent with other similar studies [Moucha *et al.*, 2007; Ghosh *et al.*, 2010]. However, Zhong and Davies [1999] indicated that the effect of LVV is dependent on mantle structure itself. For example, it was found that 3-D viscosity derived from slab models could affect degree-2 geoid [Zhong and Davies, 1999].

It is of interest to examine the effect of 3-D viscosity or LVV on the geoid for dynamically self-consistent convection models such as those in this study. To address this issue, we compute the geoid using the buoyancy structure of our convection models but with a horizontally averaged viscosity (i.e., 1-D) structure (e.g., Figure 3c) and compare the resulting geoid with the geoid using 3-D viscosity. We use Case 2 as an example for our analysis, but the results for other cases are similar. The geoid kernels for degrees 2–20 are computed for 1-D viscosity structure for Case 2 (Figure 3c) using a propagator matrix method [e.g., Hager and O'Connell, 1981] (Figure 16c). These geoid kernels are similar to those from Hager and Richards [1989], except in the upper mantle. The difference is mainly caused by the lack of a weak asthenosphere from 100 km to 400 km depths in our convection models (Figure 3c). The self-gravitational effects and an improved treatment of the boundary conditions at the CMB in our models (see section 2.3) also contribute to the difference.

The geoid kernels are convolved with buoyancy for Case 2 (e.g., Figures 10d and 11) to compute the geoid. The resulting geoid with 1-D viscosity, H_{1-D} , (Figure 16a) shows a similar degree-2 pattern to the original geoid of Case 2 with 3-D viscosity, H_{3-D} , (Figure 9e). The power spectra of H_{1-D} and H_{3-D} , as well as their degree correlations are shown in Figures 16d and 16e, respectively. While the two geoids agree very well at degree 2, significant difference exists at short wavelengths for degrees 6 and up especially for the amplitude. At degrees 3 and 4, the amplitudes of the geoid from H_{1-D} are smaller than those from H_{3-D} by 14% and 18%, respectively, but the degree correlation at degree 3 is smaller than 0.6. Because of the degree-2 dominance, the total degree correlation for degrees 2–12 between H_{1-D} and H_{3-D} is 92% and the total amplitude of H_{1-D} is 90% of H_{3-D} . The results suggest that the degree-2 geoid is not affected by LVV, consistent with what has been suggested for seismically based geoid models [e.g., Zhang and Christensen, 1993; Moucha *et al.*, 2007; Ghosh *et al.*, 2010]. However, the effect of LVV may remain significant for shorter wavelengths even for degree 3, further confirming that the effect of LVV is dependent on buoyancy/viscosity structure [Zhong and Davies, 1999].

We now go back to the compensation effect caused by heavy chemical piles for the model with 1-D viscosity. We repeat the geoid analysis for Case 2 using the 1-D viscosity (Figure 3c) and the geoid kernel approach and find that the degree-2 geoid compensation effect still exists but with a compensation layer thickness of 900 km, instead of 1200 km for the original Case 2 with 3-D viscosity. The geoid using the 1-D viscosity but with the bottom 900 km of the buoyancy structure removed (Figure 16b), H_{1-DR} , agrees with the geoid with the whole mantle buoyancy, H_{1-D} (Figure 16a), except at degree 3 where the degree correlation is

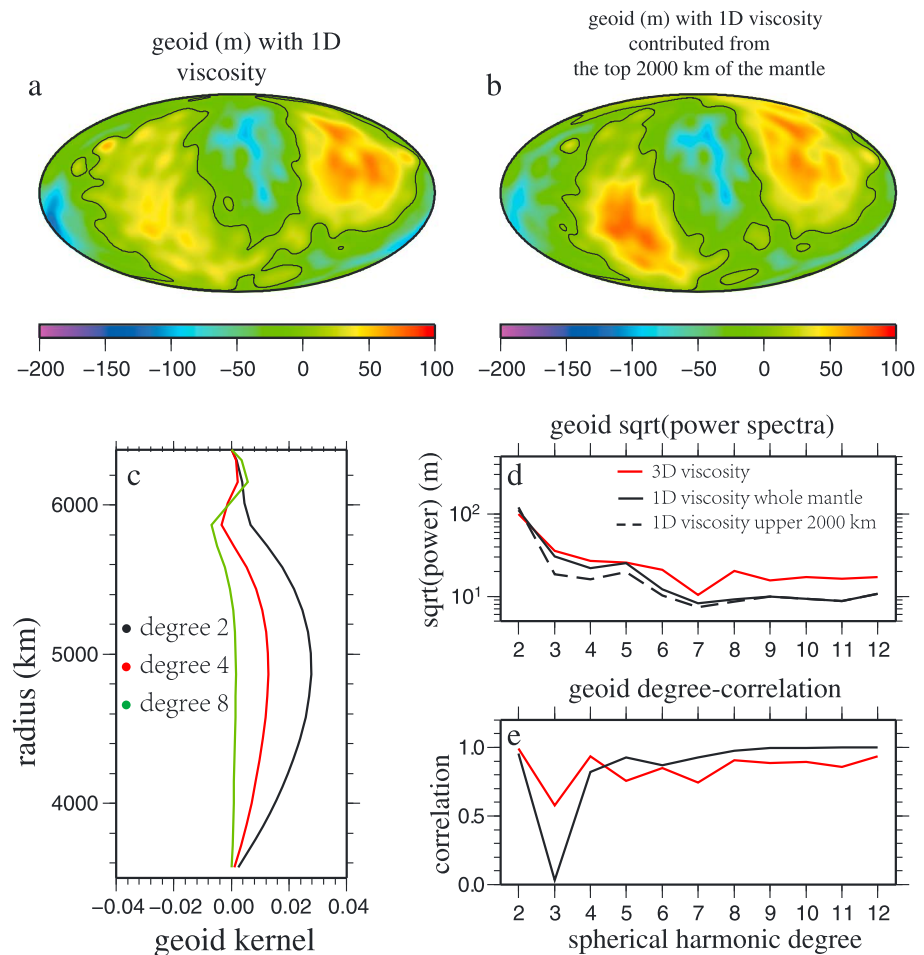


Figure 16. The geoid for Case 2 with 1-D viscosity contributed from (a) the whole mantle and (b) the top 2000 km of the mantle (i.e., excluding the bottom 900 km); (c) the geoid kernels for degrees 2 (black), 4 (red), and 8 (green) for the 1-D viscosity profile; (d) the square root of the geoid power spectra for degrees 2–12 for the original geoid with 3-D viscosity (i.e., Figure 9e) (red line), the geoid in Figure 16a (black solid line), and the geoid in Figure 16b (the black dashed line); and (e) the degree correlation for degrees 2–12 between the original geoid with 3-D viscosity and the geoid in Figure 16a (red line) and the correlation between the geoid in Figure 16a and the geoid in Figure 16b (black line). The 1-D viscosity is the horizontally averaged viscosity of the selected snapshot of Case 2 (Figure 3c).

poor (Figure 16e). This suggests that the compensation effect observed in the numerical models with 3-D viscosity also stands in geoid models with 1-D viscosity and, to the first order, can be analyzed using 1-D viscosity geoid models.

4.5. Some Potential Drawbacks of the Model

Our study represents the first attempt to investigate the geoid for thermochemical mantle convection based on dynamically self-consistent models with a number of important features that are relevant for the present-day Earth’s mantle, including degree-2 dominant structure, temperature- and depth-dependent viscosity, and chemically distinct LLSVPs. However, our models also fall short to incorporate some other features that may be potentially important for understanding the geoid. For example, tectonic plates do not emerge from our models (see discussion in section 2.2). Therefore, our models, even if they display dominantly degree-2 convective structure, do not have linear plate boundaries with localized deformation nor sheet-like downwellings (i.e., subducted slabs). Future studies are needed to examine the effects of tectonic plates on our results. In spite of recent progress in modeling mantle convection with tectonic plates [e.g., Moresi and Solomatov, 1998; Coltice et al., 2012], this type of modeling remains a significant challenge due to our poor understanding of lithospheric rheology [e.g., Zhong and Watts, 2013].

Our models do not produce positive geoid anomalies over cold downwellings. However, the Earth has geoid highs both over Africa and Pacific at degrees 2 and 3 originated from the long-wavelength lower mantle structure, and over subduction slabs, at wavelengths corresponding to degrees 4 to 9 [e.g., *Hager and Richards, 1989*]. In the Pacific, the geoid high over subduction zones is likely influenced by both subduction and lower mantle structures, and radial viscosity profile across the mantle as well as regional rheological structure might play a role. Assuming a 1-D viscosity structure, *Hager [1984]* showed that the geoid highs over subduction zones and also on global scale could be reproduced with a viscosity jump of a factor of 30 at the 670 km depth. *Moresi and Gurnis [1996]* demonstrated that for subducted slabs with higher viscosity than the ambient mantle as expected from temperature-dependent viscosity, a larger viscosity contrast (~60–200) at the 670 km depth would be required to reproduce regional geoid high over subduction zones in the western Pacific. Recently, *Hines and Billen [2012]* suggested that due to yielding-induced lateral variations of viscosity within slabs, the geoid over subduction zones might only be sensitive to local rheological structure (e.g., the mantle wedge). Our models, while producing long-wavelength mantle structure (e.g., degree 2), do not have sheet-like slabs, and this makes it difficult to account for the subduction zone geoid as observed. Future studies should explore models explaining the geoid at both global (i.e., degrees 2 and 3 for the LLSVPs) and regional scales (i.e., subduction zones) in Earth-like dynamically self-consistent models.

Phase changes are not included in our numerical models. The phase changes in the upper part of the mantle, i.e., the olivine to spinel phase change at 410 km depth and spinel to postspinel phase change at 660 km depth, may not affect significantly the large-scale mantle dynamics, especially in the lower mantle, given that the Clapeyron slope of the postspinel phase change is only ~ -2.5 MPa/K [e.g., *Fukao et al., 2009*]. The postperovskite (pPv) phase change occurs in the relatively cold slabs several hundred kilometers above the CMB and could potentially affect the lower mantle structure [e.g., *Sidorin et al., 1999; Murakami et al., 2004; Garnero and McNamara, 2008; Tosi et al., 2009*]. The pPv phase change would increase the negative buoyancy of the slabs and may weaken the slabs. However, its overall dynamic effect on the dynamics of thermochemical piles in the CMB regions is relatively minor [e.g., *Li et al., 2014b*]. We think that the effect of the pPv phase change on our results may be compensated by increasing slightly buoyancy number B for thermochemical piles in our models.

Finally, our models do not consider the effects of secular cooling including the cooling of the mantle and core, which leads to time-dependent Ra . However, we think that these effects are likely small on our results. The secular cooling is on a much longer time scale (e.g., at a cooling rate of ~ 70 K Ga⁻¹ for the mantle for the last 3 Ga [*Jaupart et al., 2007*]) than that for convective mantle structure change (Figure 2b) [*Zhong et al., 2007*].

5. Conclusion

We have computed a series of 3-D spherical convection models for both purely thermal and thermochemical convection. These dynamically self-consistent models include temperature- and depth-dependent viscosities. By varying the lithosphere viscosity, these models achieve a stable degree-2 dominant convective structure that is similar to the present-day Earth's mantle. We computed the geoid anomalies and analyzed the geoid contributed from the buoyancy structure at different depths from these models. The results can be summarized as follows:

1. Our dynamically self-consistent thermochemical convection models show that degree-2 positive geoid anomalies can be produced over chemically dense piles, which suggests that the positive long-wavelength geoid anomalies observed in the Pacific and Africa are consistent with the interpretation of the two LLSVPs as chemically dense, possibly primitive thermochemical piles. However, our degree-2 purely thermal convection models also produce positive geoid anomalies over the two major upwelling systems, consistent with previous studies of the geoid in isochemical, whole mantle models using buoyancy derived from seismic models.
2. Our dynamic models show that the chemically dense piles have a compensation effect on the surface geoid, resulting in a compensation layer at the bottom of the mantle that is 2 to 3 times as thick as the chemical piles or ~ 1000 km thick. The buoyancy in the compensation layer has zero net contribution to the surface geoid.

3. Thermochemical piles in our dynamic models have a passive and secondary effect on large-scale convective structure that is controlled by mantle viscosity structure and convection above the thermochemical piles.
4. The CMB topography is smooth and slightly negative in the regions with thermochemical piles, but significant and rapid variations in CMB topography occur outside the chemical pile regions where both the largest depression and uplifts at the CMB are found. The largest CMB depression is always under major downwellings, but the largest uplift at the CMB is near the chemical piles.
5. The 3-D viscosity or lateral variations in viscosity may not affect degree-2 geoid but may influence shorter-wavelength geoid. Our results further confirm that the effects of lateral variations in viscosity are dependent on 3-D buoyancy/viscosity structure themselves.

Acknowledgments

This work was funded by the National Science Foundation through grant 1135382. CitcomS is available through the Computational Infrastructure for Geodynamics (geodynamics.org). Calculations in this study utilized the Janus supercomputer operated by the University of Colorado Boulder and the Stampede supercomputer operated by the Texas Advanced Computing Center. We thank Rhodri Davies and an anonymous reviewer for their constructive reviews.

References

- Becker, T. W., and L. Boschi (2002), A comparison of tomographic and geodynamic mantle models, *Geochem. Geophys. Geosyst.*, *3*(1), 1003, doi:10.1029/2001GC000168.
- Boyet, M., and R. W. Carlson (2005), Nd-142 evidence for early (>4.53 Ga) global differentiation of the silicate Earth, *Science*, *309*, 576–581.
- Bunge, H. P., M. A. Richards, and J. R. Baumgardner (1996), Effect of depth-dependent viscosity on the planform of mantle convection, *Nature*, *379*, 436–438.
- Coltice, N., T. Rolf, P. J. Tackley, and S. Labrosse (2012), Dynamic causes of the relation between area and age of the ocean floor, *Science*, *336*, 335–338.
- Davaille, A. (1999), Simultaneous generation of hotspots and superswells by convection in a heterogeneous planetary mantle, *Nature*, *402*, 756–760.
- Davies, D. R., J. H. Davies, O. Hassan, K. Morgan, and P. Nithiarasu (2007), Investigations into the applicability of adaptive finite element methods to two-dimensional infinite Prandtl number thermal and thermochemical convection, *Geochem. Geophys. Geosyst.*, *8*, Q05010, doi:10.1029/2006GC001470.
- Davies, D. R., S. Goes, J. H. Davies, B. S. A. Schuberth, H.-P. Bunge, and J. Ritsema (2012), Reconciling dynamic and seismic models of Earth's lower mantle: The dominant role of thermal heterogeneity, *Earth Planet. Sci. Lett.*, *353*, 253–269, doi:10.1016/j.epsl.2012.08.016.
- Davies, G. F. (1999), *Dynamic Earth: Plates, Plumes and Mantle Convection*, 458 pp., Cambridge Univ. Press, New York.
- Davies, G. F., and F. Pribac (1993), Mesozoic seafloor subsidence and the Darwin Rise, past and present, in *The Mesozoic Pacific: Geology, Tectonics, and Volcanism*, pp. 39–52, AGU, Washington, D. C.
- Dziewonski, A. (1984), Mapping the lower mantle: Determination of lateral heterogeneity in P-velocity up to degree and order 6, *J. Geophys. Res.*, *89*, 5929–5952, doi:10.1029/JB089iB07p05929.
- Forte, A. M., and J. X. Mitrovica (2001), Deep-mantle high-viscosity flow and thermochemical structure inferred from seismic and geodynamic data, *Nature*, *410*, 1049–1056.
- Fukao, Y., M. Obayashi, and T. Nakakuki (2009), Stagnant Slab: A Review, *Annu. Rev. Earth Planet. Sci.*, *37*, 19–46, doi:10.1146/annurev.earth.36.031207.124224.
- Garnero, E. J., and A. K. McNamara (2008), Structure and dynamics of Earth's lower mantle, *Science*, *320*, 626–628, doi:10.1126/science.1148028.
- Ghosh, A., T. W. Becker, and S. J. Zhong (2010), Effects of lateral viscosity variations on the geoid, *Geophys. Res. Lett.*, *37*, L01301, doi:10.1029/2009GL040426.
- Gordon, R., and D. Jurdy (1986), Cenozoic global plate motions, *J. Geophys. Res.*, *91*, 2389–2406, doi:10.1029/JB091iB12p12389.
- Hager, B. (1984), Subducted slabs and the geoid: Constraints on mantle rheology and flow, *J. Geophys. Res.*, *89*, 6003–6015, doi:10.1029/JB089iB07p06003.
- Hager, B., and M. Richards (1989), Long-wavelength variations in Earth's geoid: Physical models and dynamical implications, *Philos. Trans. R. Soc. Math. Phys. Sci.*, *328*, 309–327.
- Hager, B., and R. O'Connell (1981), A simple global-model of plate dynamics and mantle convection, *J. Geophys. Res.*, *86*, 4843–4867, doi:10.1029/JB086iB06p04843.
- Hager, B., R. Clayton, M. Richards, R. Comer, and A. Dziewonski (1985), Lower mantle heterogeneity, dynamic topography and the geoid, *Nature*, *313*, 541–546.
- He, Y., and L. Wen (2009), Structural features and shear-velocity structure of the "Pacific Anomaly", *J. Geophys. Res.*, *114*, B02309, doi:10.1029/2008JB005814.
- He, Y., and L. Wen (2012), Geographic boundary of the "Pacific Anomaly" and its geometry and transitional structure in the north, *J. Geophys. Res.*, *117*, B09308, doi:10.1029/2012JB009436.
- Hernlund, J. W., and C. Houser (2008), The statistical distribution of seismic velocities in Earth's deep mantle, *Earth Planet. Sci. Lett.*, *265*, 423–437, doi:10.1016/j.epsl.2007.10.042.
- Hines, J. M., and M. I. Billen (2012), Sensitivity of the short- to intermediate-wavelength geoid to rheologic structure in subduction zones, *J. Geophys. Res.*, *117*, B05410, doi:10.1029/2011JB008978.
- Hofmann, A. W. (1997), Mantle geochemistry: The message from oceanic volcanism, *Nature*, *385*, 219–229.
- Houser, C., G. Masters, P. Shearer, and G. Laske (2008), Shear and compressional velocity models of the mantle from cluster analysis of long-period waveforms, *Geophys. J. Int.*, *174*, 195–212, doi:10.1111/j.1365-246X.2008.03763.x.
- Huang, J., and G. F. Davies (2007), Stirring in three-dimensional mantle convection models and implications for geochemistry: Passive tracers, *Geochem. Geophys. Geosyst.*, *8*, Q03017, doi:10.1029/2006GC001312.
- Jaupart, C., S. Labrosse, and J.-C. Mareschal (2007), Temperatures, heat and energy in the mantle of the Earth, *Treatise Geophys.*, *7*, 253–303.
- Jellinek, A. M., and M. Manga (2002), The influence of a chemical boundary layer on the fixity, spacing and lifetime of mantle plumes, *Nature*, *418*, 760–763.
- Kellogg, L. H., B. H. Hager, and R. D. van der Hilst (1999), Compositional stratification in the deep mantle, *Science*, *283*, 1881–1884.
- King, S. D., and G. Masters (1992), An inversion for radial viscosity structure using seismic tomography, *Geophys. Res. Lett.*, *19*, 1551–1554, doi:10.1029/92GL01700.

- Kunz, J., T. Staudacher, and C. J. Allegre (1998), Plutonium-fission xenon found in Earth's mantle, *Science*, *280*, 877–880.
- Lassak, T. M., A. K. McNamara, E. J. Garnero, and S. Zhong (2010), Core-mantle boundary topography as a possible constraint on lower mantle chemistry and dynamics, *Earth Planet. Sci. Lett.*, *289*, 232–241.
- Leng, W., and S. Zhong (2011), Implementation and application of adaptive mesh refinement for thermochemical mantle convection studies, *Geochem. Geophys. Geosyst.*, *12*, Q04006, doi:10.1029/2010GC003425.
- Lerch, F. J., S. M. Klosko, and G. B. Patel (1983), *A Refined Gravity Model From Lageos (GEM2)*, NASA Technical Memorandum 84986, Goddard Space Flight Center, Greenbelt/Maryland.
- Li, Y., F. Deschamps, and P. J. Tackley (2014a), The stability and structure of primordial reservoirs in the lower mantle: Insights from models of thermochemical convection in three-dimensional spherical geometry, *Geophys. J. Int.*, *199*, 914–930, doi:10.1093/gji/ggu295.
- Li, Y., F. Deschamps, and P. J. Tackley (2014b), Effects of low-viscosity post-perovskite on the stability and structure of primordial reservoirs in the lower mantle, *Geophys. Res. Lett.*, *41*, 7089–7097, doi:10.1002/2014GL061362.
- Lithgow-Bertelloni, C., and P. G. Silver (1998), Dynamic topography, plate driving forces and the African superswell, *Nature*, *395*, 269–272, doi:10.1038/26212.
- Marty, J., and A. Cazenave (1989), Regional variations in subsidence rate of oceanic plates: A global analysis, *Earth Planet. Sci. Lett.*, *94*, 301–315.
- Masters, G., S. Johnson, G. Laske, and H. Bolton (1996), A shear-velocity model of the mantle, *Philos. Trans. R. Soc. Math. Phys. Sci.*, *354*, 1385–1410.
- Masters, G., G. Laske, H. Bolton, and A. Dziewonski (2000), The relative behavior of shear velocity, bulk sound speed, and compressional velocity in the mantle: Implications for chemical and thermal structure, in *Earth's Deep Interior: Mineral Physics and Tomography From the Atomic to the Global Scale*, pp. 63–87, AGU, Washington, D. C.
- McNamara, A. K., and S. J. Zhong (2004a), The influence of thermochemical convection on the fixity of mantle plumes, *Earth Planet. Sci. Lett.*, *222*, 485–500.
- McNamara, A. K., and S. J. Zhong (2004b), Thermochemical structures within a spherical mantle: Superplumes or piles?, *J. Geophys. Res.*, *109*, B07402, doi:10.1029/2003JB002847.
- McNamara, A. K., and S. J. Zhong (2005a), Thermochemical structures beneath Africa and the Pacific Ocean, *Nature*, *437*, 1136–1139.
- McNamara, A. K., and S. J. Zhong (2005b), Degree-one mantle convection: Dependence on internal heating and temperature-dependent rheology, *Geophys. Res. Lett.*, *32*, L01301, doi:10.1029/2004GL021082.
- Mitrovica, J. X., and A. M. Forte (2004), A new inference of mantle viscosity based upon joint inversion of convection and glacial isostatic adjustment data, *Earth Planet. Sci. Lett.*, *225*, 177–189, doi:10.1016/j.epsl.2004.06.005.
- Moresi, L., and M. Gurnis (1996), Constraints on the lateral strength of slabs from three-dimensional dynamic flow models, *Earth Planet. Sci. Lett.*, *138*, 15–28.
- Moresi, L., and V. Solomatov (1998), Mantle convection with a brittle lithosphere: Thoughts on the global tectonic styles of the Earth and Venus, *Geophys. J. Int.*, *133*, 669–682.
- Moucha, R., A. M. Forte, J. X. Mitrovica, and A. Daradich (2007), Lateral variations in mantle rheology: Implications for convection related surface observables and inferred viscosity models, *Geophys. J. Int.*, *169*, 113–135, doi:10.1111/j.1365-246X.2006.03225.x.
- Murakami, M., K. Hirose, K. Kawamura, N. Sata, and Y. Ohishi (2004), Post-perovskite phase transition in MgSiO₃, *Science*, *304*, 855–858, doi:10.1126/science.1095932.
- Ni, S. D., E. Tan, M. Gurnis, and D. Helmberger (2002), Sharp sides to the African superplume, *Science*, *296*, 1850–1852.
- Oldham, D., and J. H. Davies (2004), Numerical investigation of layered convection in a three-dimensional shell with application to planetary mantles, *Geochem. Geophys. Geosyst.*, *5*, Q12C04, doi:10.1029/2003GC000603.
- Pekeris, C. L. (1935), The propagation of Rayleigh waves in heterogeneous media, *Phys. J. Gen. Appl. Phys.*, *6*, 133–138.
- Ratcliff, J. T., P. J. Tackley, G. Schubert, and A. Zebib (1997), Transitions in thermal convection with strongly variable viscosity, *Phys. Earth Planet. Inter.*, *102*, 201–212.
- Ricard, Y., M. Richards, C. Lithgow-Bertelloni, and Y. Lestunff (1993), A geodynamic model of mantle density heterogeneity, *J. Geophys. Res.*, *98*, 21,895–21,909, doi:10.1029/93JB02216.
- Richards, M. A., and B. H. Hager (1989), Effects of lateral viscosity variations on long-wavelength geoid anomalies and topography, *J. Geophys. Res.*, *94*, 10,299–10,313, doi:10.1029/89JB00718.
- Ritsema, J., H. J. van Heijst, and J. H. Woodhouse (1999), Complex shear wave velocity structure imaged beneath Africa and Iceland, *Science*, *286*, 1925–1928.
- Romanowicz, B., and Y. C. Gung (2002), Superplumes from the core-mantle boundary to the lithosphere: Implications for heat flux, *Science*, *296*, 513–516.
- Schuberth, B. S. A., H.-P. Bunge, and J. Ritsema (2009), Tomographic filtering of high-resolution mantle circulation models: Can seismic heterogeneity be explained by temperature alone?, *Geochem. Geophys. Geosyst.*, *10*, Q05W03, doi:10.1029/2009GC002401.
- Schuberth, B. S. A., C. Zoroli, and G. Nolet (2012), Synthetic seismograms for a synthetic Earth: Long-period P- and S-wave travel-time variations can be explained by temperature alone, *Geophys. J. Int.*, *188*, 1393–1412, doi:10.1111/j.1365-246X.2011.05333.x.
- Sidorin, I., M. Gurnis, and D. V. Helmberger (1999), Evidence for a ubiquitous seismic discontinuity at the base of the mantle, *Science*, *286*, 1326–1331, doi:10.1126/science.286.5443.1326.
- Simons, M., and B. H. Hager (1997), Localization of the gravity field and the signature of glacial rebound, *Nature*, *390*, 500–504, doi:10.1038/37339.
- Steinberger, B., and T. H. Torsvik (2010), Toward an explanation for the present and past locations of the poles, *Geochem. Geophys. Geosyst.*, *11*, Q06W06, doi:10.1029/2009GC002889.
- Su, W. J., and A. M. Dziewonski (1997), Simultaneous inversion for 3-D variations in shear and bulk velocity in the mantle, *Phys. Earth Planet. Inter.*, *100*, 135–156.
- Tackley, P. J. (1998), Three-dimensional simulations of mantle convection with a thermochemical CMB boundary layer: D?, in *The Core-Mantle Boundary Region, Geodynamics Series*, pp. 231–253, AGU, Washington, D. C.
- Tackley, P. J., and S. D. King (2003), Testing the tracer ratio method for modeling active compositional fields in mantle convection simulations, *Geochem. Geophys. Geosyst.*, *4*, 8302, doi:10.1029/2001GC000214.
- Tanimoto, T. (1990), Long-wavelength S-wave velocity structure throughout the mantle, *Geophys. J. Int.*, *100*, 327–336.
- Tosi, N., O. Cadek, Z. Martinez, D. A. Yuen, and G. Kaufmann (2009), Is the long-wavelength geoid sensitive to the presence of postperovskite above the core-mantle boundary?, *Geophys. Res. Lett.*, *36*, L05303, doi:10.1029/2008GL036902.
- van Keken, P. E., S. D. King, H. Schmeling, U. R. Christensen, D. Neumeister, and M. P. Doin (1997), A comparison of methods for the modeling of thermochemical convection, *J. Geophys. Res.*, *102*, 22,477–22,495, doi:10.1029/97JB01353.

- van Keken, P. E., C. J. Ballentine, and D. Porcelli (2001), A dynamical investigation of the heat and helium imbalance, *Earth Planet. Sci. Lett.*, *188*(3–4), 421–434.
- Wang, Y., and L. X. Wen (2004), Mapping the geometry and geographic distribution of a very low velocity province at the base of the Earth's mantle, *J. Geophys. Res.*, *109*, B10305, doi:10.1029/2003JB002674.
- Wen, L. X., P. Silver, D. James, and R. Kuehnel (2001), Seismic evidence for a thermo-chemical boundary at the base of the Earth's mantle, *Earth Planet. Sci. Lett.*, *189*, 141–153.
- Wu, W., S. Ni, and Z. Shen (2014), Constraining the short scale core-mantle boundary topography beneath Kenai Peninsula (Alaska) with amplitudes of core-reflected PcP wave, *Phys. Earth Planet. Inter.*, *236*, 60–68, doi:10.1016/j.pepi.2014.09.001.
- Zhang, N., S. Zhong, W. Leng, and Z. X. Li (2010), A model for the evolution of the Earth's mantle structure since the early Paleozoic, *J. Geophys. Res.*, *115*, B06401, doi:10.1029/2009JB006896.
- Zhang, S. X., and U. Christensen (1993), Some effects of lateral viscosity variations on geoid and surface velocities induced by density anomalies in the mantle, *Geophys. J. Int.*, *114*, 531–547, doi:10.1111/j.1365-246X.1993.tb06985.x.
- Zhong, S., and A. B. Watts (2013), Lithospheric deformation induced by loading of the Hawaiian Islands and its implications for mantle rheology, *J. Geophys. Res.-Solid Earth*, *118*, 6025–6048, doi:10.1002/2013JB010408.
- Zhong, S. J., and G. F. Davies (1999), Effects of plate and slab viscosities on the geoid, *Earth Planet. Sci. Lett.*, *170*, 487–496, doi:10.1016/S0012-821X(99)00124-7.
- Zhong, S. J., M. T. Zuber, L. Moresi, and M. Gurnis (2000), Role of temperature-dependent viscosity and surface plates in spherical shell models of mantle convection, *J. Geophys. Res.*, *105*, 11,063–11,082, doi:10.1029/2000JB900003.
- Zhong, S., N. Zhang, Z. X. Li, and J. H. Roberts (2007), Supercontinent cycles, true polar wander, and very long-wavelength mantle convection, *Earth Planet. Sci. Lett.*, *261*, 551–564.
- Zhong, S., A. McNamara, E. Tan, L. Moresi, and M. Gurnis (2008), A benchmark study on mantle convection in a 3-D spherical shell using CitcomS, *Geochem. Geophys. Geosyst.*, *9*, Q10017, doi:10.1029/2008GC002048.